

Fermion disorder operator: the hedgehog and the fox of quantum many-body entanglement

Weilun Jiang,^{1,2} Bin-Bin Chen,^{3,*} Zi Hong Liu,⁴ Junchen Rong,⁵
Fakher F. Assaad,⁴ Meng Cheng,⁶ Kai Sun,⁷ and Zi Yang Meng^{3,†}

¹*Beijing National Laboratory for Condensed Matter Physics and Institute of Physics, Chinese Academy of Sciences, Beijing 100190, China*

²*School of Physical Sciences, University of Chinese Academy of Sciences, Beijing 100190, China*

³*Department of Physics and HKU-UCAS Joint Institute of Theoretical and Computational Physics,
The University of Hong Kong, Pokfulam Road, Hong Kong SAR, China*

⁴*Institut für Theoretische Physik und Astrophysik and Würzburg-Dresden Cluster
of Excellence ct.qmat, Universität Würzburg, 97074 Würzburg, Germany*

⁵*Institut des Hautes Études Scientifiques, 91440 Bures-sur-Yvette, France*

⁶*Department of Physics, Yale University, New Haven, CT 06520-8120, USA*

⁷*Department of Physics, University of Michigan, Ann Arbor, Michigan 48109, USA*

(Dated: April 11, 2023)

As the saying goes “The fox knows many things but the hedgehog knows one big thing”, here we show that the disorder operator is both the fox and the hedgehog in probing the many aspects of quantum entanglement in fermionic many-body systems. From both analytical and numerical computations in free and interacting fermion systems in 1d and 2d, we find the disorder operator and the entanglement entropy exhibit similar universal scaling behavior, as a function of the boundary length of the subsystem, but with subtle yet important differences. In 1D they both follow the $\log L$ scaling behavior with the coefficient determined by the Luttinger parameter for the case of disorder operator, and the conformal central charge for entanglement entropy. In 2D they both show the universal $L \log L$ scaling behavior in free and interacting Fermi liquid phases, with the coefficients depending on the geometry of the Fermi surfaces. However, at a 2d quantum critical point, extra symmetry information is needed in the design of the disorder operator to be able to reveal the critical fluctuations as does in the entanglement entropy. Our results demonstrate the fermion disorder operator can be used to probe certain aspects of quantum many-body entanglement related to global symmetry, and provide new tools to explore the still largely unknown territory of highly entangled fermion quantum matter in 2 or higher dimensions.

I. INTRODUCTION

There is a line dated back to the ancient Greek poet Archilochus: “The fox knows many things, but the hedgehog knows one big thing.” This saying later becomes extremely popular thanks to the famous essay by Isaiah Berlin, in which he expanded upon this idea to divide writers and thinkers into the categories of hedgehog or fox, in which the former such as Plato, Confucius, Dante, Hegel, Nietzsche, Dostoevsky, etc, view the world through the lens of a single defining idea and the latter such as Lao-Tze, Aristotle, Shakespeare, Goethe, Balzac, Joyce, etc, draw on a wide variety of experiences and for whom the world cannot be boiled down to a single idea [1].

Tolstoy, with his voluminous assessments of literature and human thoughts, goes beyond such fox-hedgehog classification paradigm. According to Berlin’s analysis, Tolstoy’s talents are those of a fox while his beliefs are ought to be a hedgehog. It is this duality – by nature a fox but a hedgehog by conviction – made the greatness of the writer but also caused great pain to him at the later part of his life.

In recent years, quantum many-body entanglement has become a subject of intense activity, and one fundamental question is to find ways to probe one big, or many different aspects of many-body entanglement in quantum matter. The most familiar probes include non-local measurements such as the von Neumann and Rényi entanglement entropy (EE), the

entanglement spectrum (ES) and bipartite fluctuations, which have been studied in many different types of quantum many-body systems [2–18]. Recently, along this line, it has been proposed that concept of the *disorder operator* may provide an effective tool for capturing some aspects of the entanglement information, especially the interplay with global symmetry [19–26]. In a variety of systems, universal quantities, such as the logarithmic corner corrections in (2+1)d conformal field theories [16, 21, 25], and defect quantum dimensions in gapped phases [26], were successfully extracted from the scaling behavior of the disorder operators. Compared to EE, the computational cost of the disorder operators is often significantly reduced, which allows for access to much larger size and reduced finite-size effect.

In this paper, we would like to expand upon these developments and demonstrate that, the disorder operator can be utilized to probe many-body entanglement in fermion systems, again with computational simplicity and reliable data quality. As will be shown below, they obey similar scaling laws as that of EEs. However, there are important differences between the disorder operator and EE, since by construction the disorder operator measures the symmetry charge contained in a region, while the EE is not directly related to any global symmetry. In a way, the fermion disorder operator is similar with Tolstoy as being both a fox and a hedgehog in Berlin’s essay – probing the universal entanglement by nature but also subjected to the symmetry details by construction – and it is in this duality that the fermion disorder operator exhibits itself as a new and promising vehicle with which we could explore the territory of quantum entanglement in two or higher dimensional

* bchenhku@hku.hk

† zymeng@hku.hk

interacting fermion systems.

We begin the narrative with a brief discussion about the development of computational scheme and the known scaling behavior of EE. In general, the Rényi EE can be measured via the replica trick [5] in the path-integral quantum Monte Carlo (QMC) simulations. More concretely, for the n -th order Rényi entropy S_n , one creates n copies of the system (i.e. replicas), properly connected along the entanglement cut, and measures the correlation between the replicas [27]. Due to the n fold expansion of the configuration space and the nontrivial connectivity between the replicas during the sampling processes, obtaining numerical data of EE with good quality in QMC simulations has remained a very challenging task. Despite the difficulty, we note there are recent progresses in the nonequilibrium incremental algorithm to obtain the S_n with high efficiency and precision [16, 18, 28, 29] and similar advance in measuring the ES [17] in QMC simulations, which effectively solve the difficulties in measuring EE in boson/spin systems in 2+1d (that can be efficiently simulated by QMC methods).

However, progress in the extraction of entanglement information in interacting fermion systems has largely fallen behind. In the fermion QMC simulation for EE, one could likewise calculate the joint probability [12] by constructing the extended manifold for ensemble average [13–15]. But the necessity of using replica renders the already difficult determinant QMC simulation (DQMC, usually the computational complexity scales as $O(\beta N^3)$ with $\beta = 1/T$ and $N = L^d$ for the d spatial dimension) even heavier, and such computational burden, along with the associated limitation in 2d interacting fermion systems with accessible systems $L < 100$, have hinged the widespread usage and discussion of the scaling behavior of EE in the exploration of the highly entangled fermionic quantum matter.

In this work, we show that the disorder operator offers an numerically easier way to access certain aspects of quantum many-body entanglement in interacting fermionic systems. We design the disorder operators to probe the charge and spin fluctuations in the entangled subregion and show that they exhibit similar scaling behavior as that of EE. In fact, for non-interacting fermions (Rényi) EE can be exactly expressed in terms of charge disorder operators. However, in contrast to the EE measurement with additional numerical complexities due to replicas, the disorder operator is an equal-time observable with no need for extended manifold and substantially reduces the computational complexity. We find the fermion disorder operators share the good properties of its bosonic cousin [21, 22, 25, 26] and demonstrate their applications in several representative classes of fermionic systems, including the free Fermi surface (FS), Luttinger liquid (LL) in 1D, and a 2D lattice model of spin-1/2 fermions interacting with Ising spins which exhibit both the Fermi liquid (FL) phases and non-Fermi liquid (nFL) quantum critical point (QCP) separating symmetric and symmetry-breaking FLs.

It is interesting to find that, although similar with the EE in some ways, the disorder operator is a distinct observable with its own characters. For example in a 1d LL, the charge disorder operator has a $\log L$ scaling form, and the coefficient is the charge Luttinger parameter, whereas that of the EE is the cen-

tral charge. In the 2D interacting FL, numerically we observe that both the disorder operator and the EE only receive very small deviation compared with their values in the free system, and show the same $L_M \log L_M$ scaling where L_M is the linear size of the subregion M . This deviation does not seem to increase with the size L_M , indicating that in the large L_M limit, both disorder operator and EE remain $L_M \log L_M$, with coefficients very close to the free values. At the QCP, we find the deviation of the EE from the free theory increases with L_M , which suggests that the scaling form of EE might be different. As for the disorder operator, the result depends strongly on which type of symmetry it probes. For the charge symmetry, the disorder operator behaves like the one far away from QCP. For the spin one, which is related with the symmetry-breaking channel of the particular QCP we looked at, the coefficient of the $L_M \log L_M$ term increases drastically at the QCP. These results show the hedgehog and fox duality in the fermion disorder operator and demonstrate that it can indeed capture the universal and various entanglement properties in the interesting yet difficult interacting fermion systems.

II. SUMMARY OF KEY RESULTS

Here we summarize key conclusions of our study. For free fermions, we showed that charge/spin disorder operator directly measures the quantum entanglement. For example, the second Rényi entropy S_2 is identical to the log of the charge (spin) disorder operator at angle $\frac{\pi}{2}$ ($\theta = \pi$):

$$S_2 = -2 \log \left| X^\rho \left(\frac{\pi}{2} \right) \right| = -2 \log |X^\sigma(\pi)|. \quad (1)$$

More general relations between Rényi entropies S_n and the disorder operators are given in Eqs. (8)- (10) in Sec. IV A. For a Fermi sea ground state, it is well-known that $S_2 \sim L_M^{d-1} \ln L_M$, where d is the spatial dimension and L_M is the linear size of the subregion M used to define the disorder operator and/or the EE. For generic values of θ , the charge/spin disorder operator obeys the same functional form. The coefficient of the $L_M^{d-1} \log L_M$ term, which is proportional to θ^2 , is fully consistent with analytic form based on the Widom-Sobolev formula [Eq.(15)] [30–33].

For interacting fermions in 1D, we find that both Rényi entropies S_n and the log of the disorder operators $-\log |X^\rho(\theta)|$ follow the same functional form $\sim \log L_M$, same as the free fermion system, but with different coefficients. It is well-known that the $\log L_M$ -term coefficient of the EE measures the central charge. We will find that the coefficient of the charge/spin disorder operator gives the Luttinger parameter in the charge/spin sector. Utilizing DMRG and DQMC, we find that disorder operator offers a highly efficient way to measure the Luttinger parameter. In comparison to more conventional approaches based on structure factors at small momentum, the disorder operator exhibits much less finite-size effect, and can provide highly accurate estimates of Luttinger parameters with low numerical costs.

For 2D interacting fermions, we studied an itinerant fermion systems, whose phase diagram shows a continuous

quantum phase transition between a paramagnetic phase and an Ising ferromagnetic phase [34–37]. Away from the QCP, the system is a FL, while in the quantum critical regime, critical fluctuations drive the system into a nFL [36, 38]. We computed the charge and spin disorder operator, as well as the second Rényi entropy using DQMC. The simulations indicate that within numerical error, S_2 and $-\log |X_M^\rho|$ obey the same functional form $\sim L_M \log L_M$ as non-interacting fermions. For the spin disorder operator, because spin S^z is the order parameter of this quantum phase transition, the coefficient of the $L_M \log L_M$ term appears to diverge near the QCP, supposedly due to the divergent critical fluctuations. As for the charge disorder operator $-\log |X_M^\rho|$ and S_2 , no singular behavior is observed near the QCP. Instead, the values of $-\log |X_M^\rho|$ and S_2 remain very close to the free-fermion formula [Eq.(15)], and the deviation is less than a couple percent.

Although the observed deviation from the non-interacting case is small, it is not zero. More careful analysis reveals that as interactions becomes stronger (getting close to the QCP), interaction effect increases the value of S_2 and decreases the value of $-\log |X_M^\rho|$. This effect is beyond the numerical error bar, and more importantly, finite-size scaling analysis shows that this deviation does not disappear as the system size increases, suggesting that it may survive in the thermodynamic limit. More precisely, deviations of $-\log |X_M^\rho|$ from the results of the free system appear to saturate at large system size, both in the FL phase and in the nFL near the QCP. This observation indicate that $-\log |X_M^\rho|$ still scales as $L_M \log L_M$, same as the non-interacting Fermi sea, but the coefficient of the $L_M \log L_M$ term decreases as interactions becomes stronger, both in the FL phase and at the QCP. For S_2 , away from the QCP, its deviation from the free theory saturate at large system size, and thus we expect the relation $S_2 \sim L_M \log L_M$ survives in the FL phase, with a coefficient increasing as interaction gets stronger. At the QCP (i.e., a nFL), the deviation of S_2 from the non-interacting value does not seem to saturate, up to the largest system size that we can assess. Due to the limitation of system sizes, we cannot pinpoint the precise functional form of S_2 at the QCP. If the deviation eventually saturates as the system size increases further, it would imply that $S_2 \sim L_M \log L_M$ at the QCP, although with a significant enhancement of the coefficient. If the deviation keeps increasing with larger system sizes, it means S_2 grows faster than $L_M \log L_M$ at large L_M .

III. THE DISORDER OPERATOR

In a fermionic system with conserved particle number, the corresponding charge U(1) symmetry allows us to define a charge disorder operator

$$\hat{X}_M^\rho(\theta) = \prod_{i \in M} e^{i\theta \hat{n}_i} = e^{i\theta \hat{N}_M} \quad (2)$$

where \hat{n}_i is the particle number operator at lattice site i , and \hat{N}_M is the total particle number operator of region M , as shown in the schematic plots in Fig. 3 (b) and (d).

If the system is composed of spin-1/2 fermions and has an U(1) spin conservation, e.g., spin rotations around the z axis, we can further define a spin disorder operator

$$\hat{X}_M^\sigma(\theta) = \prod_{i \in M} e^{i\theta \hat{S}_i^z} = e^{i\theta \hat{S}_M^z} \quad (3)$$

where $\hat{S}_i^z = \frac{1}{2}(\hat{n}_{i\uparrow} - \hat{n}_{i\downarrow})$ is the z -component of the spin operator at lattice site i , and \hat{S}_M^z is the total spin z -component of region M .

For convenience, we denote $X_M(\theta) = \langle \hat{X}_M(\theta) \rangle$, where $\langle \cdot \rangle$ is the ground state expectation value. The computation of X_M as an equal-time observable in DQMC is discussed in the Sec. I of the Supplemental Material (SM) [39]. It is straightforward to prove that if the system is divided into two parts M and \bar{M} and assume the ground state preserves the symmetry, $|X_M^{\rho/\sigma}(\theta)| = |X_{\bar{M}}^{\rho/\sigma}(\theta)|$, in analogy with EE. In addition, the disorder operator also obeys the following relations: $X_M^\rho(\theta) = X_M^\rho(\theta + 2\pi)$, $X_M^\sigma(\theta) = X_M^\sigma(\theta + 4\pi)$, $X_M^{\rho,\sigma}(\theta) = X_M^{\rho,\sigma}(-\theta)^*$, and $X_M^{\rho,\sigma}(0) = 1$. In the small θ limit, $X_M^{\rho/\sigma}$ measures the density/spin fluctuations in the region M : $-\log |X_M^\rho(\theta)|/\theta^2 = \langle (\hat{N}_M - \langle \hat{N}_M \rangle)^2 \rangle$ [22] and $-\log |X_M^\sigma(\theta)|/\theta^2 = \langle (\hat{S}_M^z - \langle \hat{S}_M^z \rangle)^2 \rangle$.

For non-interacting fermions, the disorder operators can be calculated using the equal-time Green's function

$$G_{i\sigma,j\sigma'} = \langle \hat{c}_{i\sigma} \hat{c}_{j\sigma'}^\dagger \rangle, \quad (4)$$

where $\hat{c}_{i\sigma}$ and $\hat{c}_{j\sigma'}^\dagger$ are fermion annihilation and creation operator at sites i and j respectively, and σ and σ' are the spin indices. Define the matrix $G_M = G_{i\sigma,j\sigma'}$ with i and j confined to a region M . The charge disorder operators for the region M can be written as a matrix determinant

$$X_M^\rho(\theta) = \det [G_M + (\mathbb{1} - G_M)e^{i\theta}] , \quad (5)$$

where $\mathbb{1}$ represents the identity matrix. For spin-1/2 fermions with U(1) spin conservation, the Green's function G_M breaks down into spin up and down sectors $G_{M,\uparrow}$ and $G_{M,\downarrow}$, and thus the disorder operator can be written as

$$X_M^\rho(\theta) = \det [X_{M,\uparrow}(\theta) X_{M,\downarrow}(\theta)] \quad (6)$$

$$X_M^\sigma(\theta) = \det \left[X_{M,\uparrow} \left(\frac{\theta}{2} \right) X_{M,\downarrow} \left(-\frac{\theta}{2} \right) \right] \quad (7)$$

where $X_{M,\sigma}(\theta) = G_{M,\sigma} + (\mathbb{1} - G_{M,\sigma})e^{i\theta}$ for $\sigma = \uparrow, \downarrow$. For non-interacting systems, $\det (X_{M,\uparrow} X_{M,\downarrow})$ can be factorized into $\det X_{M,\uparrow} \det X_{M,\downarrow}$, and thus the spin and charge disorder operators obey a simple relation $|X_M^\rho(\theta)| = |X_M^\sigma(2\theta)|$.

IV. NON-INTERACTING LIMIT

In this section, we study non-interacting systems, where an explicit connection between the disorder operator $X_M^\rho(\theta)$ and the Rényi entropy S_n can be analytically proved. Besides the mathematical proof, we will also demonstrate and verify these relations numerically in concrete models, before exploring interacting systems.

A. Exact relations between disorder operator and EE

For non-interacting systems, the Rényi entropy S_n can be exactly related to the disorder operator $X_M^\rho(\theta)$. For S_2 and S_3 , we have

$$S_2 = -2 \log \left| X_M^\rho \left(\frac{\pi}{2} \right) \right|, \quad (8)$$

$$S_3 = -\log \left| X_M^\rho \left(\frac{2\pi}{3} \right) \right|. \quad (9)$$

For general values of n ,

$$\begin{aligned} S_n &= \frac{1}{1-n} \sum_{\alpha=0}^{n-1} \log X_M^\rho \left(\left[\frac{1+(-1)^n}{2} + 2\alpha \right] \frac{\pi}{n} \right) \\ &= \frac{2}{1-n} \sum_{\alpha=0}^{2\alpha+1 < n} \log \left| X_M^\rho \left(\left[\frac{1+(-1)^n}{2} + 2\alpha \right] \frac{\pi}{n} \right) \right|. \end{aligned} \quad (10)$$

In the presence of U(1) spin conservation, these relations also apply to spin disorder operators X_M^σ , but the values of θ change, e.g., $S_2 = -2 \log |X_M^\sigma(\pi)|$.

Detailed proof of these relations can be found in Sec. II of the SM [39]. Here, we just briefly outline the idea. It has been shown that the Rényi entropy can be calculated using the cumulants of charge fluctuations $C^k = (-i\partial_\theta)^k \log X_M^\rho(\theta)|_{\theta=0}$ [11, 40], which is the key reason why disorder operators can give the value of the Rényi entropy. In addition, to obtain a simple relation between S_n and X_M^ρ , we express both these two quantities in terms of equal-time fermion Green's functions $G_{i\sigma,j\sigma'}$, utilizing Wick's theorem for S_n [11, 12] and the Levitov-Lesovik determinant formula [41–43] for X_M^ρ . After some manipulations described in the SM [39], the relations above can be obtained. Besides, the relation between the reduced density matrix with the equal time Green's functions is deduced in Ref. [44]. Refer to this equation, S_n is expressed with Green's functions in Ref. [12].

B. The disorder operator and EE for 1D non-interacting fermions

In this section, we demonstrate the scaling behavior of the disorder operators in a 1D non-interacting fermion model with periodic boundary conditions (PBCs). For simplicity, we focus on spinless fermions, and utilize Eq. (5) to compute the disorder operator. This calculation can be easily generalized to non-interacting spin-1/2 fermions with U(1) spin conservation, where the charge and spin disorder operator $X_M^\rho(\theta) = X_M^\uparrow(\theta)X_M^\downarrow(\theta)$ and $X_M^\sigma(\theta) = X_M^\uparrow(\frac{\theta}{2})X_M^\downarrow(-\frac{\theta}{2})$, and each spin sector can be treated as spinless fermions.

The Hamiltonian of this model is

$$\hat{H} = -t_1 \sum_{\langle i,j \rangle} \hat{c}_i^\dagger \hat{c}_j - \mu \sum_i \hat{n}_i, \quad (11)$$

where the nearest-neighbor hopping strength t_1 is set to unity and the chemical potential μ is between ± 2 to ensure a partially filled band. We choose M to be an interval of the 1D

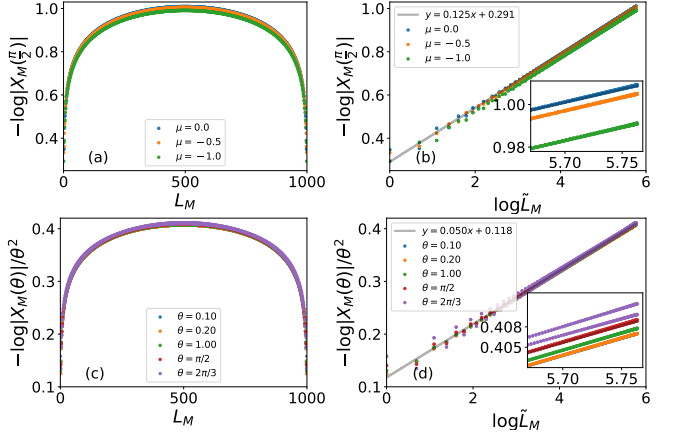


FIG. 1. (a) and (b) The disorder operator $-\log |X_M(\frac{\pi}{2})|$ of a 1D free fermion chain at various μ . Here we use the PBC and the system size is $L = 1000$. In (b), we fit the data to the functional form $-\log |X_M(\frac{\pi}{2})| = s_{1d}(\frac{\pi}{2}) \log \tilde{L}_M + \text{const}$, where $\tilde{L}_M = \frac{L}{\pi} \sin \frac{\pi L_M}{L}$ is the conformal distance. The grey line shows the best fitting for $\mu = 0$ at $\log \tilde{L}_M > 2$. Upon varying μ , we find that the constant part in the fitting varies [see the inset panel in Fig.(b)], but the value of $s_{1d}(\frac{\pi}{2})$ is universal ~ 0.125 , in full agreement with theory prediction $s_{1d}(\frac{\pi}{2}) = 1/8$. In (c) and (d), we plot $-\log |X_M(\theta)|/\theta^2$ at various θ for $\mu = 0$. In the large size limit, the leading order contribution $\sim \log \tilde{L}_M$ is found to be independent of θ . In panel (d), the grey line shows the best fitting for $\theta = 0.1$ at $\log \tilde{L}_M > 2$, which gives the slope 0.050, in good agreement with the theory prediction $\frac{1}{2\pi^2} \approx 0.051$.

chain with length L_M , and plot $-\log |X_M(\theta)|$ as a function of L_M in Fig. 1. Because $|X_M| = |X_{\overline{M}}|$, the function is necessarily symmetric with respect to $L_M = \frac{L}{2}$, with L being the system size [Fig. 1(a) and (c)]. In the regime $a \ll L_M \ll L$, where a is the lattice constant, the leading term of $-\log |X_M|$ exhibits a universal scaling relation $-\log |X_M| = s_{1d}(\theta) \log L_M + O(1)$, and the data suggests that the coefficient $s_{1d}(\theta)$ is independent of the chemical potential $-2 < \mu < 2$.

In order to obtain a more accurate fitting for the coefficient $s(\theta)$, here we introduce the conformal distance $\tilde{L}_M = \frac{L}{\pi} \sin \frac{\pi L_M}{L}$, and replace the fitting form $-\log |X_M| = s_{1d}(\theta) \log L_M + O(1)$ with $-\log |X_M| = s_{1d}(\theta) \log \tilde{L}_M + O(1)$. In the regime of $1 \ll L_M \ll L$, \tilde{L}_M coincides with L_M and thus the two fitting formulas are interchangeable. However, as L_M approaches $\frac{L}{2}$ or becomes larger than $\frac{L}{2}$, the introduction of the conformal length greatly suppresses non-universal subleading terms and thus provides a much more accurate value for s_{1d} . As shown in Fig. 1(b) and (d), the relation $-\log |X_M| \sim s_{1d}(\theta) \log \tilde{L}_M$ holds for a very wide region from L_M , except for the data points with L_M very close to 1 or L . For the coefficient s_{1d} , in principle, it can be written as a power-law expansion $s_{1d}(\theta) = S_2 \theta^2 + S_4 \theta^4 + \dots$, where the coefficients S_k can be obtained from the corresponding cumulants of charge fluctuations $C^k = (-i\partial_\theta)^k \log X_M^\rho(\theta)|_{\theta=0}$ is [11, 40]. The coefficient S_2 can be calculated exactly, using density-density correlations $S_2 = \frac{1}{2\pi^2}$. As for higher order

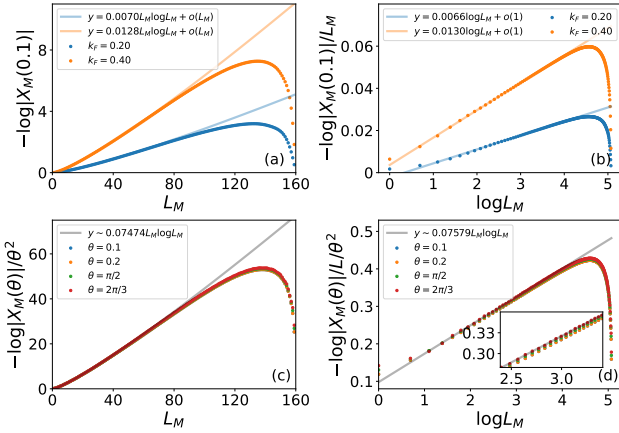


FIG. 2. (a) and (b) The disorder operator $-\log |X_M(\theta = 0.1)|$ of a 2D non-interacting Fermi gas with Fermi wavevector $k_F = 0.2$ (or $k_F = 0.4$). The model utilizes a $L \times L = 160 \times 160$ square lattice with PBCs. Here, we fit the data with $y = s_{2d}L_M \log L_M + bL_M + c$ in (a) and $y = s_{2d} \log L_M + b$ in (b), which is expected for the regime $1 \ll L_M \ll L$. Here, we used points with $L_M \in [10, 30]$ for the fitting. The value of s_{2d} obtained from the fitting is consistent with the analytic analysis $s_{2d} = k_F \theta^2 / \pi^3$. (c) $-\log |X_M(\theta)|/\theta^2$ with $t_1 = 1, t_2 = 0, \mu = -0.5$ for various θ s. The two sets of data overlays on top of each other, indicating $s_{2d} \propto \theta^2$. The solid lines are fittings using $y = s_{2d}L_M \log L_M + bL_M + c$ for (c) and $y = s_{2d} \log L_M + b$ for (d), for points with $L_M \in [10, 30]$ to avoid the finite size effect.

terms (S_k with $k > 2$), the Widom-Sobolev formula suggests that they shall all vanish, $S_k = 0$ for $k > 2$ [40]. Therefore, we shall expect

$$-\log |X_M(\theta)| = \frac{\theta^2}{2\pi^2} \log L_M + O(1) \quad (12)$$

for $-\pi < \theta < \pi$. For $\theta > \pi$ or $\theta < -\pi$, the value of $-\log |X_M(\theta)|$ can be obtained using the periodic condition $X_M(\theta) = X_M(\theta + 2\pi)$.

As shown in Fig. 1(b) and(d), the numerical fitting indeed supports the analytic result and the Widom-Sobolev formula. We find that $s_{1d}(\theta)/\theta^2$ is a constant ~ 0.050 , independent of the value of θ , and this value is very close to the theoretical expectation $S_2 = \frac{1}{2\pi^2} \approx 0.051$.

To further verify Eq. (12), we used this formula to compute the Rényi EE. By plugging in Eq. (12) into Eqs. (8)- (10), we find that $S_2 = \frac{1}{4} \log L_M + O(1)$, $S_3 = \frac{2}{9} \log L_M + O(1)$, and $S_n = \frac{1}{6}(1 + \frac{1}{n}) \log L_M + O(1)$. This result fully agrees with the Rényi entropy formula of 1D free fermions $S_n = \frac{c}{6}(1 + \frac{1}{n}) \log L_M + O(1)$, where $c = 1$ is the conformal central charge of 1D spinless fermions.

C. Disorder operator and EE for 2D non-interacting fermions

In this section, we study 2D free fermions with a FS. Here we use a square lattice model with nearest-neighbor (t_1) and

next-nearest-neighbor hoppings (t_2). The Hamiltonian is

$$\hat{H} = -t_1 \sum_{\langle i,j \rangle} \hat{c}_i^\dagger \hat{c}_j - t_2 \sum_{\langle\langle i,j \rangle\rangle} \hat{c}_i^\dagger \hat{c}_j - \mu \sum_i \hat{n}_i \quad (13)$$

And we choose a square region M as shown in Fig. 3(d).

For a 2D FL with a circular-shaped FS, the disorder operator at the small θ limit can be calculated exactly (See Sec. IV of SM [39])

$$-\log |X_M(\theta)| = \frac{k_F \theta^2}{\pi^3} L_M \log L_M + O(L_M) \quad (14)$$

where k_F is the Fermi wave-vector. In Fig. 2 (a) and (b), we compare this analytic prediction with numerically obtained $|X_M(\theta)|$. We study two different cases with a nearly circular FS, one with $k_F \approx 0.4$ ($t_1 = 1, t_2 = 0, \mu = -3.84$) and the other with $k_F \approx 0.2$ ($t_1 = 1, t_2 = 0, \mu = -3.96$), and obtain the coefficients $s(\theta)$ by fitting the data with the formula $-\log |X_M(\theta)| = s_{2d}(\theta)L_M \log L_M + b \log L_M + c$. Although the FS deviates slightly from a perfect circle, the fitted values of $s_{2d}(\theta)$ are very close to the analytic formula Eq (14).

In general, when the FS is not a perfect circle but still share the same topology, the disorder operator can be calculated using the Widom-Sobolev formula [30–33, 40],

$$-\log |X_M(\theta)| = \frac{\theta^2}{4\pi^2} \lambda_M L_M^{d-1} \log L_M + O(L_M^{d-1}) \quad (15)$$

where the prefactor λ_M is defined as

$$\lambda_M = \iint \frac{dA_x dA_k |n_x \cdot n_k|}{(2\pi)^{d-1}}. \quad (16)$$

Here n_x and n_k are unit normal vectors of the real space boundary of M and the momentum space boundary of FS, respectively. The double integral goes over the boundary of M and the boundary of the Fermi sea. For a circular FS, this formula recovers Eq. (14) above. Note that λ_M is a pure geometric quantity, determined by the shape of M and the FS.

Our numerical fitting is in full support the Widom-Sobolev formula. In the regime $a \ll L_M \ll L$, we find $-\log |X_M(\theta)| \sim s_{2d}(\theta)L_M \log L_M$ and $s_{2d}(\theta) \propto \theta^2$ [Fig. 2 (c) and (d)], and the constant ratio $s_{2d}(\theta)/\theta^2$ is in agreement with the integral in Eq. (15). In addition, we have also verified the connection between $|X_M(\theta)|$ and the Rényi EE. Using Eq. (15) and Eqs. (8)- (10), we get

$$S_2 = \frac{\lambda_M}{8} L_M \log L_M + O(L_M), \quad (17)$$

$$S_3 = \frac{\lambda_M}{9} L_M \log L_M + O(L_M), \quad (18)$$

$$S_n = \frac{1 + n^{-1}}{12} \lambda_M L_M \log L_M + O(L_M). \quad (19)$$

This result is fully consistent with free-fermion EE obtained from the Widom-Sobolev formula [30–33, 40, 45, 46].

V. DISORDER OPERATOR IN INTERACTING FERMION SYSTEMS

For interacting fermions, the exact relation between EE and disorder operator [Eqs. (8)- (10)] is no longer valid, but there still exists interesting connection between these two quantities in their implementation in DQMC simulations.

A. DQMC relation between disorder operator and EE

To demonstrate this connection, here we use some auxiliary field $\{s\}$ to decouple the interactions between fermions such that we transform the interacting fermion problem into an equivalent model where fermions couple to this auxiliary field $\{s\}$, which mediate interactions between fermions. This is how DQMC is implemented to simulate interacting fermion models. In this setup, the expectation value of a physics quantity can be written as $\langle O \rangle = \sum_{\{s\}} P_s \langle O \rangle_s$, where $\sum_{\{s\}}$ sums

over all auxiliary field configurations; P_s is the probability distribution of auxiliary field configurations; and $\langle O \rangle_s$ can be viewed as the expectation value of O for an static auxiliary field configuration s .

Here, we focus on the relation between S_2 and $X_M^\rho(\frac{\pi}{2})$ [Eq. (8)]. Using the auxiliary field approach shown above, the disorder operator can be written as

$$X_M^\rho(\theta) = \sum_{\{s\}} P_s \det [G_M + (\mathbb{1} - G_M)e^{i\theta}], \quad (20)$$

where $G_{M,s}$ is the equal-time fermion Green's function for the auxiliary field configuration s . In the non-interacting limit, there is no need to introduce the auxiliary field, i.e., G_M is independent of s and thus Eq. (20) recovers the free fermion formula Eq. (5) at $\theta = \frac{\pi}{2}$.

Utilizing Eq. (20), we can write down the following formula for interacting fermions

$$\begin{aligned} -2 \log |X_M^\rho(\frac{\pi}{2})| &= -\log \left\{ \sum_{\{s\}} P_s \det [G_{M,s} + i(\mathbb{1} - G_{M,s})] \times \sum_{\{s'\}} P_{s'} \det [G_{M,s'} - i(\mathbb{1} - G_{M,s'})] \right\} \\ &= -\log \left\{ \sum_{\{s,s'\}} P_s P_{s'} \det [G_{M,s} G_{M,s'} + (\mathbb{1} - G_{M,s})(\mathbb{1} - G_{M,s'}) + i(G_{M,s} - G_{M,s'})] \right\} \end{aligned} \quad (21)$$

where $\{s, s'\}$ label independent auxiliary field configurations. For the Rényi entropy S_2 , as shown in Ref. [12], we have

$$S_2 = -\log \left\{ \sum_{\{s,s'\}} P_s P_{s'} \det [G_{M,s} G_{M,s'} + (\mathbb{1} - G_{M,s})(\mathbb{1} - G_{M,s'})] \right\}. \quad (22)$$

By comparing Eqs. (21) and (22), we can see that $-2 \log |X_M^\rho(\frac{\pi}{2})|$ and S_2 only differs by one term $i(G_{M,s} - G_{M,s'})$. For non-interacting fermions, G_M is independent of auxiliary field s and thus this term vanishes. As a result, we find $S_2 = -2 \log |X_M^\rho(\frac{\pi}{2})|$ for non-interacting particles as shown in Eq. (8). For interacting particles, in general this relation between S_2 and $X_M^\rho(\frac{\pi}{2})$ no longer holds. Below, we study two interacting models (in 1D and 2D respectively) to explore the difference and connection between these two quantities.

B. Disorder operator and S_2 in a Luttinger liquid

Let us study disorder operator in a 1D spinless LL [47]. The Hamiltonian can be written as

$$H_L = \frac{v_F}{2\pi} \int dx [K(\partial_x \vartheta)^2 + K^{-1}(\partial_x \phi)^2]. \quad (23)$$

Here v_F is the Fermi velocity, K is the Luttinger parameter. We follow the convention that the left/right-moving fermion fields are bosonized as $\psi_{R/L}(x) \sim e^{-i[\pm\phi(x) - \vartheta(x)]}$. Using

the expression for the charge density $\rho(x)$

$$\rho(x) = -\frac{1}{\pi} \partial_x \phi, \quad (24)$$

we can easily compute the disorder operator:

$$\left\langle \exp \left(i\theta \int_0^{L_M} dx \rho(x) \right) \right\rangle = \langle e^{\frac{i\theta}{\pi} [\phi(0) - \phi(L_M)]} \rangle \sim L_M^{-\frac{\theta^2 K}{2\pi^2}}. \quad (25)$$

Therefore

$$-\ln |X_M(\theta)| \sim \frac{\theta^2 K}{2\pi^2} \ln L_M + \dots \quad (26)$$

The non-interacting Hamiltonian corresponds to $K = 1$ and we indeed reproduce the result in Eq. (12).

Now let us generalize to interacting spin- $\frac{1}{2}$ electrons [47]. Following standard practice in bosonization we introduce

$$\begin{aligned} \phi_\rho(x) &= \frac{1}{\sqrt{2}} [\phi_\uparrow(x) + \phi_\downarrow(x)], \\ \phi_\sigma(x) &= \frac{1}{\sqrt{2}} [\phi_\uparrow(x) - \phi_\downarrow(x)], \end{aligned} \quad (27)$$

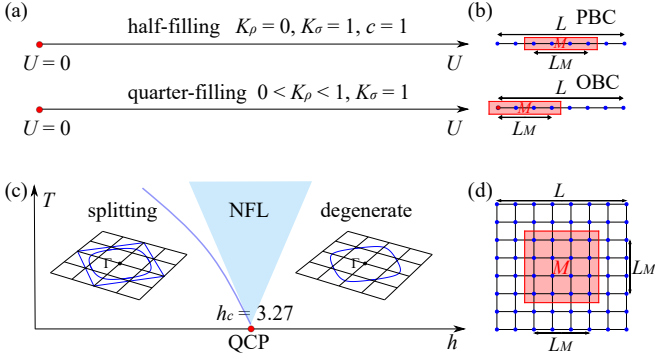


FIG. 3. (a) The zero temperature phase diagram of Hubbard chain at half- and quarter- fillings. The Luttinger parameters and conformal central charge are shown. (b) The entangling subregion M (red) in the system with PBC and OBC, where M contains L_M lattice sites. (c) The T - h phase diagram of the 2D interacting fermion model, where fermions couple to ferromagnetic Ising spins with a transverse field h . As shown in Refs. [34–36], $h > h_c$ is the paramagnetic phase where spin up and down fermions are degenerate and share the same FS. For $h < h_c$, the model has an itinerant ferromagnetic phase, where spin-up and down FSs splits. $h = h_c$ is the QCP that separate these two phases, where critical fluctuations destroy the coherence of fermionic particles and result in a nFL phase with fermion self-energy scales as $\sim \omega_n^{2/3}$ [36]. (d) The entangling region M (red) defined on a $L \times L$ square lattice with PBC, where M contains $L_M \times L_M$ sites.

and similarly ϑ_ρ and ϑ_σ . The Hamiltonian now reads

$$H = \sum_{\alpha=\rho,\sigma} \frac{v_\alpha}{2\pi} \int dx [K_\alpha (\partial_x \vartheta_\alpha)^2 + K_\alpha^{-1} (\partial_x \phi_\alpha)^2]. \quad (28)$$

Here K_ρ and K_σ are the Luttinger parameters of the charge and spin channels, respectively. In models with SU(2) spin rotation symmetry (e.g. the Hubbard model), the Luttinger parameter $K_\sigma = 1$ to preserve the SU(2) symmetry. With the bosonization formula we can easily compute the charge disorder operators:

$$\begin{aligned} -\ln |X_M^\rho(\theta)| &= -\ln | \langle e^{\frac{\sqrt{2}i\theta}{\pi}(\phi_\rho(0)-\phi_\rho(L_M))} \rangle | \\ &= \frac{\theta^2 K_\rho}{\pi^2} \ln L_M + \dots, \end{aligned} \quad (29)$$

and similarly for the spin channel:

$$\begin{aligned} -\ln |X_M^\sigma(\theta)| &= -\ln | \langle e^{\frac{i\theta}{4\pi}(\phi_\sigma(0)-\phi_\sigma(L_M))} \rangle | \\ &= \frac{\theta^2 K_\sigma}{4\pi^2} \ln L_M + \dots, \end{aligned} \quad (30)$$

In a 1D LL, the 2nd Rényi entropy S_2 is given by $S_2 = \frac{c}{4} \log L_M + \dots$. Notice that the coefficient of the log term does not depend on Luttinger parameters at all. On the other hand, as we have just shown the disorder operators, while having similar logarithmic scaling with L_M , strongly depend on Luttinger parameters and eventually interactions (especially X_M^ρ).

To demonstrate this difference, here we consider a 1D repulsive Hubbard chain

$$H_U = -t \sum_{\langle ij \rangle, \sigma} \hat{c}_{i\sigma}^\dagger \hat{c}_{j\sigma} + U \sum_i \hat{n}_{i\uparrow} \hat{n}_{i\downarrow}. \quad (31)$$

At half-filling, the ground state of this model has a charge gap ($\Delta_c \sim e^{-t/U}$ when U small), while the spin degrees of freedom remain gapless [48]. For the charge disorder operator, since $K_\rho = 0$ we expect $-\log |X_M^\rho(\theta)|$ to be a constant without log correction. Whereas for the spin disorder operator we should have $-\log |X_M^\sigma(\theta)| = \frac{\theta^2}{4\pi^2} \log L_M + \text{const.}$. For EE, we expect $S = \frac{c}{4} \log L_M + \text{const.}$, with $c = 1$ due to the gapless spin channel.

We compute the disorder operator with $\theta = \frac{\pi}{2}$ and EE in the $L = 64$ chains with PBC to the high precision via DMRG and DQMC simulations. As shown in Fig. 4(a), at $U = 3$, the disorder operator and EE behave as expected, that is, the disorder operator becomes a plateau in the bulk as $K_\rho = 0$, and EE show a clear $\log L_M$ dome-like behavior due to $c = 1$. In Fig. 4(b), we further verify this by plotting EE and disorder operator versus the conformal distance \tilde{L}_M , and the slopes of the darker blue and red data give central charge $c \simeq 1.009$ and $K_\rho \simeq 0.004$, well consistent with our expectation.

As a byproduct, we find the disorder operator serves as a highly efficient tool for extracting Luttinger parameters. Traditionally, in DMRG simulations, the K_α is determined from the structure factor $S_\alpha(k) \sim \frac{K_\alpha}{\pi} |k|$ at $k \rightarrow 0$, where $\alpha = \rho$ or σ , representing the charge or spin sector. For systems with a small gap, this approach can suffer from serious finite-size effects, making it very challenging to obtain the correct values of K_α . Specifically, for the half-filled Hubbard chain studied here, because the charge gap closes exponentially as U decreases towards zero, an exponentially large system size L is required to overcome the finite-size effect to obtain K_ρ . For example, as shown in Ref. [50], at $U = 1.6$, the conventional approach gives a wrong value of $K_\rho \sim 0.5$ at half-filling, even with system size as large as $L = 512$ (See also Sec. V in SM [39]). In contrast, if we fit the disorder operator with its scaling form $-\log |X_M^\rho(\frac{\pi}{2})| = \frac{K_\rho}{4} \log L_M + \text{const}$, the finite-size effect is much less severe. As shown in Fig. 4 (c,d), with $L = 256$, this fitting is already sufficient to provide the value of K_ρ with high accuracy at and away from half filling. From this fitting, we get $K_\rho \simeq 0.001$ and $K_\rho \simeq 0.819$ at half and quarter fillings ($n = 1$ and $n = 0.5$) respectively, in perfect agreement with exact results from the Bethe ansatz: $K_\rho = 0$ at half-filling and $K_\rho \simeq 0.82$ at quarter filling [49]. In Fig. 4 (e,f), we also check the Luttinger parameter of the spin sector K_σ for both half-filling ($n = 1$) and quarter-filling ($n = 0.5$), and find $K_\sigma \simeq 0.998$ for $n = 1$ and $K_\sigma \simeq 0.943$ for $n = 0.5$, in good agreement with the expected value $K_\sigma = 1$.

C. 2D Fermi Liquid and non-Fermi Liquid

We now move on to study the disorder operator and the EE for interacting itinerant fermions in 2D. In contrast to 1D or the non-interacting limits, where precise knowledge about the

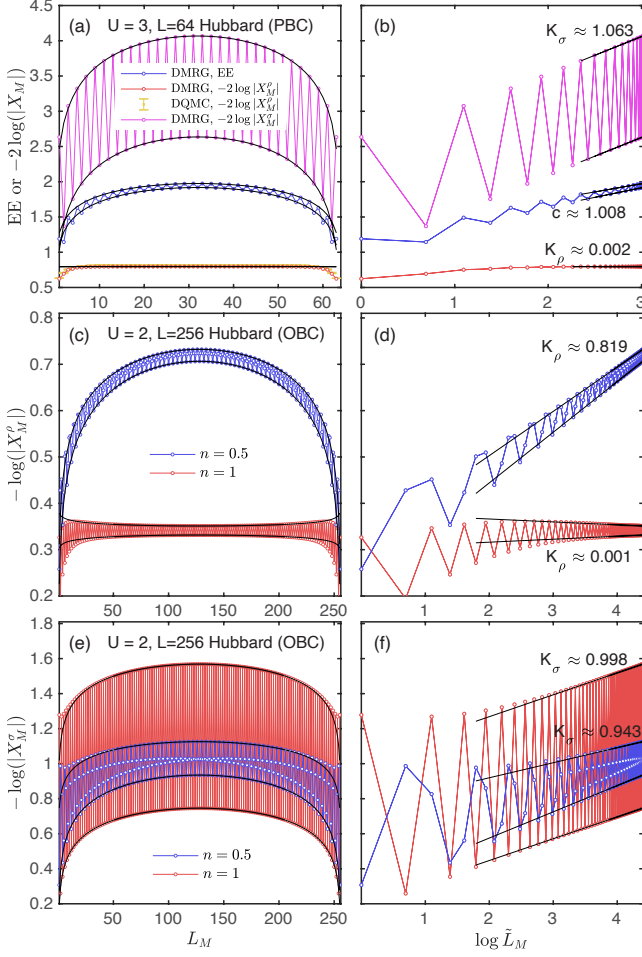


FIG. 4. (a) Rényi entropy S_2 and disorder operators, $-\log|X_M^\rho(\frac{\pi}{2})|$ and $-\log|X_M^\sigma(\pi)|$, for a half-filled Hubbard chain with PBC at $U = 3$ and system size $L = 64$. The data points are obtained via DMRG and DQMC, and the horizontal axis L_M is the size of the region M . Figure (b) shows the same data vs the log of the conformal distance $\log \tilde{L}_M = \log(\frac{L}{\pi} \sin \frac{\pi L_M}{L})$, which should be fitted to a linear function at large $\log \tilde{L}_M$, and we find that $c \approx 1.009$, $K_\rho \approx 0.004$ and $K_\sigma \approx 1.063$. (c,d) Charge disorder operator $-\log|X_M^\rho(\frac{\pi}{2})|$ in a Hubbard chain with OBC at half- or quarter- fillings. Here we utilize DMRG to compute the disorder operator and set $U = 2$ and $L = 256$. Fitting in Fig. (d) gives $K_\rho \approx 0.001$ (half filling) and $K_\rho \approx 0.819$ (quarter filling), consistent with the Bethe ansatz results $K_\rho = 0$ (half filling) and $K_\rho \approx 0.82$ (quarter filling) [49]. (e,f) Spin disorder operator $-\log|X_M^\sigma(\pi)|$ for the same model. The fitting gives $K_\sigma \approx 0.998$ for half filling and $K_\sigma \approx 0.943$ for quarter filling, consistent with the expected value $K_\sigma = 1$.

disorder operator and EE can be obtained from exact solutions and/or effective field theory, 2D itinerant fermions is a much more challenging problem with limited analytical results. In this section, we use DQMC to compute the charge- and spin-disorder operators and the second Rényi entropy, and using the numerical results to examine the connection and difference between disorder operators and the EE.

Both in theory and in DQMC simulations, a very fruitful ap-

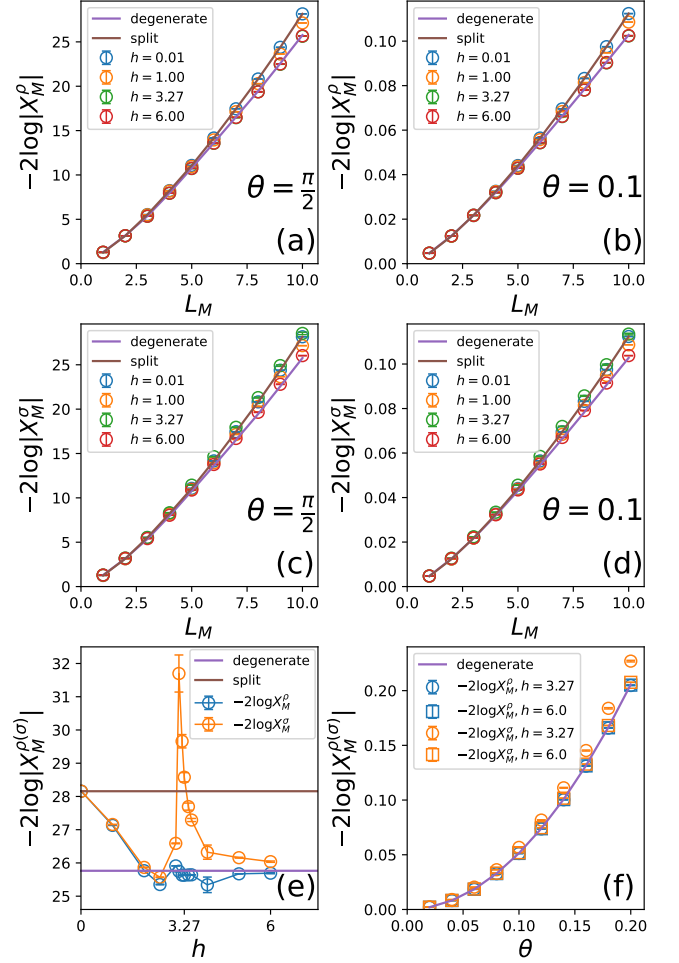


FIG. 5. The charge (a-b) and spin (c-d) disorder operators at various h with $L = 20$ and $\beta = 100$. $h_c = 3.27$ is the QCP, and $h > h_c$ ($h < h_c$) is the paramagnetic (ferromagnetic) phase. The purple (brown) solid line marks the exact formula at the noninteracting limit $h = \infty$ ($h = 0$). From (a)-(d), we find that both $-\log|X_M^\rho|$ and $-\log|X_M^\sigma|$ scale as $L_M \log L_M$. For the charge disorder operator $-\log|X_M^\rho|$, the coefficient of the $L_M \log L_M$ term is very close to the free-fermion prediction [Eq (15)]. In the paramagnetic phase and at the critical point, the FS remain degenerate, and thus $-\log|X_M^\rho|$ remains almost a constant independent of h . In the ferromagnetic phase, because the splitting between the spin up and down FSs increases as we decrease h , this change in the FS shape increases the value of $-\log|X_M^\rho|$. This trend is clearer in Fig. (e), which shows the h dependence of the disorder operator. As for the spin sector, the value of $-\log|X_M^\sigma|$ shows a sharp peak at the QCP, due to the divergent spin fluctuations, as shown in the main text. In Fig. (f), we plot the θ -dependence of disorder operator. Same as in free fermion systems, we find that both $-\log|X_M^\rho|$ and $-\log|X_M^\sigma|$ scales as θ^2 , for both the FL phase and at the QCP.

proach to access FLs and the nFLs is to couple free fermions with critical bosonic fluctuations [34–36, 51–68]. Away from the quantum critical regime, these models provide a FL phase. In the vicinity of the QCP, critical fluctuations drive the system into a nFL phase with over-damped low-energy fermionic excitations [38].

In this study, we utilize one of simplest and well-studied models of this type: spin-1/2 fermions coupled to a ferromagnetic transverse-field Ising model as studied in Refs. [34–38]. The Hamiltonian contains three parts

$$H_{\text{FS}} = H_{\text{f}} + H_{\text{Ising}} + H_{\text{int}}, \quad (32)$$

where

$$\begin{aligned} H_{\text{f}} &= -t_1 \sum_{\langle ij \rangle \sigma \lambda} (\hat{c}_{i\sigma\lambda}^\dagger \hat{c}_{j\sigma\lambda} + \text{h.c.}) - \mu \sum_{i\sigma\lambda} \hat{n}_{i\sigma\lambda}, \\ H_{\text{Ising}} &= -J \sum_{\langle ij \rangle} \hat{s}_i^z \hat{s}_j^z - h \sum_i \hat{s}_i^x, \\ H_{\text{int}} &= -\frac{\xi}{2} \sum_i \hat{s}_i^z (\hat{S}_{i,1}^z + \hat{S}_{i,2}^z). \end{aligned} \quad (33)$$

The fermionic part H_{f} consists of two identical layers of fermions labeled by the layer index $\lambda = 1, 2$, and $\sigma = \uparrow, \downarrow$ labels the fermion spin. Here, fermions can hop between neighboring sites of a square lattice (t_1) and μ is the chemical potential. The bosonic part H_{Ising} describes quantum Ising spins with ferromagnetic interactions subject to a transverse field h . They live on the same square lattice. In the absence of fermions, these Ising spins form a paramagnetic (ferromagnetic) phase if $h > h_c$ ($h < h_c$), separated by a QCP, which belongs to the 2+1D Ising universality class at $h = h_c \approx 3.04$. The last term H_{int} couples the fermion spins with Ising spins at the same lattice site. With this coupling, the paramagnetic-ferromagnetic phase transition for the Ising spins now induces a quantum phase transition for the fermions, i.e., a paramagnetic-ferromagnetic phase transition for itinerant fermions. We set $t_1 = 1$, $\mu = -0.5$, $J = 1$ and fix the coupling strength $\xi = 1$, and it has been shown that for these parameters, the QCP is located at $h_c = 3.27$ [34].

As shown in Ref. [34], the global internal symmetry of H_{FS} is identified as

$$\text{SU}(2)_\uparrow \times \text{SU}(2)_\downarrow \times \text{U}(1)_\uparrow \times \text{U}(1)_\downarrow \times \mathbb{Z}_2, \quad (34)$$

where the $\text{SU}(2)_\uparrow \times \text{SU}(2)_\downarrow$ group consists of independent rotations in the layer λ basis for each spin species of fermions. The $\text{U}(1)_\uparrow \times \text{U}(1)_\downarrow$ symmetries correspond to conservation of particle number with spin up and spin down, and the \mathbb{Z}_2 symmetry, generated by $\prod_i \hat{s}_i^x \prod_i e^{i\pi(S_{i,1}^x + S_{i,2}^x)}$, acts as $S_{i,\lambda}^z \rightarrow -S_{i,\lambda}^z$, $s_i^z \rightarrow -s_i^z$, the latter is the symmetry breaking channel and defines the order parameter of the ferromagnetic phase.

In addition, this Hamiltonian is invariant under the antiunitary symmetry $i\tau_y K$, where τ_y is a Pauli matrix in the layer basis and K is the complex conjugation operator. Thanks to this symmetry, the QMC simulation is free of sign problem [69].

Away from the QCP, the fermions form a FL with well-defined quasi-particles. In the paramagnetic phase ($h > h_c$), fermions of both spin flavors have the same FS, while in the ferromagnetic phase ($h < h_c$), the FSs for spin up and down fermions split, due to the spontaneous magnetization. Near the QCP ($h \sim h_c$), critical fluctuations gives rise to a nFL,

where fermionic excitations becomes over-damped and the FS is smeared out and the quantum part of the fermionic self-energy satisfies $\sim \omega_n^{2/3}$ [36].

From these symmetries, multiple disorder operators can be introduced: for example, the charge disorder operator shown in Eq. (2) from the U(1) charge conservation and the spin disorder operator defined in Eq. (3) due to the conservation of the z component of the fermion spin S_z . We note the Ising symmetry of H_{FS} in Eq. (32) also enables us to define this disorder operator $\hat{S}_M^z = \prod_{i \in M} s_i^x e^{i\pi(S_{i,1}^x + S_{i,2}^x)}$. In this study, however, we will focus on the charge and spin disorder operators, Eqs. (2) and (3), while other disorder operators will not be considered due to the technical challenge to measure them in DQMC. This is because the DQMC simulation utilizes the spin up and down states as the basis for both the Ising spins and fermion spins, measuring the x component of spin is costly, while for charge density and z component of the spin operator, we can access large system size up to $L \times L = 24 \times 24$ and temperature down to $\beta = 100$.

We note, in principle, the EE is not directly related to any global symmetry of the system, and as we will show below, it not only reveals the $L_M \log L_M$ scaling behavior coming from the geometry of FS in an interacting FL, but also the quantum critical scaling at QCP whose precise scaling form is still unknown. Here we see clearly that the disorder operator can indeed capture the $L_M \log L_M$ universal entanglement scaling in the interacting fermion models as that of the EE, but at the same time, extra symmetry consideration is needed, if one is asking for the particular information in the QCP entanglement.

Fig. 5(a) shows $X_M^\rho(\frac{\pi}{2})$ for $L = 20$. The model has two exactly solvable limits, $h \rightarrow \infty$ and $h \rightarrow 0$, where fermions are non-interacting, i.e., the system is a non-interacting Fermi gas. At $h \rightarrow \infty$, spin up and down fermions share the same FS, while at $h = 0$, the spin-up and down FSs split, due to the ferromagnetic order. For both these two limits, the exact solution indicate that $-\log |X_M^{\rho/\sigma}(\theta)| \sim s(\theta) L_M \log L_M$ with $s(\theta) \propto \theta^2$ and the proportionality coefficient is determined by the shapes of the region M and the FS, as shown in Eq. (15). These two exact solvable limits are shown in Fig. 5 as solid lines marked as “degenerate” ($h \rightarrow \infty$) and “split” ($h = 0$) respectively.

As shown in Fig. 5(a) and (b), for the paramagnetic phase ($h < h_c$), the charge disorder operator depends very weakly on h , and its value remains nearly the same as the non-interacting limit $h \rightarrow \infty$, even if h reaches the critical value h_c . This is very different from the 1D case, where the value of the disorder operator starts to change immediately even if an infinitesimal amount of interactions are introduced, due to the change in Luttinger parameters. This observation, if taken at the face value, seems to indicate that interactions between fermions is irrelevant for X_M^ρ , and the non-interacting formula [Eq. (15)] survives in the FL phase. However, as will be discussed below, a more careful analysis indicates the opposite. For the ferromagnetic phase ($h > h_c$), the numerical data indicates that $-\log |X_M^\rho(\theta)|$ still scales as $\theta^2 L_M \log L_M$, but with coefficient that gradually increases as we decrease h . This is again largely consistent with the non-interacting

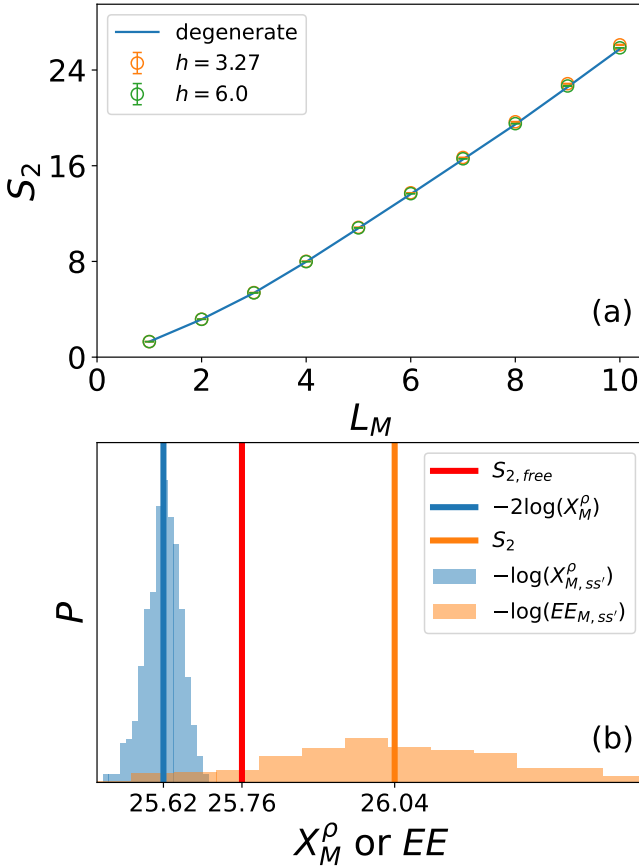


FIG. 6. (a) S_2 versus L_M at $h = h_c = 3.27$ and $h = 6.0$. The value is close to the free-fermion limit (solid line), but with some small deviations, which will be analyzed in panel (b). (b) Distribution of $EE_{M,ss'}$ and X_M^ρ over different auxiliary-field configurations. The mean values of these two quantities, after taken a log, are S_2 and $-2 \log |X_M^\rho(\frac{\pi}{2})|$, which are marked by the orange and blue vertical lines respectively. This distribution demonstrate the error bar of S_2 and $-2 \log |X_M^\rho(\frac{\pi}{2})|$, and it is clear that S_2 ($-2 \log |X_M^\rho(\frac{\pi}{2})|$) is larger (smaller) than the free-fermion limit, $S_{2,free}$ marked by the vertical red line. In contrast to free systems, where S_2 and $-2 \log |X_M^\rho(\frac{\pi}{2})|$ coincide, at QCP, we find that these two quantities clearly deviates from each other, and both of them differ from their free theory value.

formula Eq. (15). Because the FS splits in the ferromagnetic phase and this splitting increases when h reduces towards zero, the coefficient of the $L_M \log L_M$ term should shift according to the shape of the FS. This trend of X_M^ρ is summarized in Fig. 5(e).

As for the spin disorder operator, we plotted the two noninteracting limits, $h \rightarrow \infty$ and $h \rightarrow 0$, in Fig. 5(c) and (d) as the solid lines. In the non-interacting limit, $|X_M^\sigma(\theta)|$ obeys the exact identity $|X_M^\sigma(\theta)| = |X_M^\rho(\frac{\theta}{2})|$, and thus it doesn't carry any extra information beyond the charge disorder operator. For interacting fermions $0 < h < \infty$, we find that $|X_M^\sigma(\theta)|$ starts to deviate from $|X_M^\rho(\frac{\theta}{2})|$. Away from the QCP, the deviation is small. However, near the QCP a much larger deviation is observed and $-\log |X_M^\sigma(\theta)|$ shows a peak at $h \sim h_c$,

as shown in Fig. 5(e). This peak of $-\log |X_M^\sigma(\theta)|$ is due to the fact that the spin disorder operator happens to be the order parameter of this QCP. As shown early on, at small θ , $-\log |X_M^\sigma(\theta)|$ measures the fluctuations of σ_z in the region M , $-\log |X_M^\sigma(\theta)|/\theta^2 = \langle (\hat{S}_M^z - \langle \hat{S}_M^z \rangle)^2 \rangle$, which develops a peak at the QCP. The location of this peak marks the critical value of h , at which spin fluctuations are pronounced and thus can be used as a tool to detect the QCP.

In addition to the disorder operators, we also compute the second Rényi entropy S_2 . Previous variational Monte Carlo studies of EE for trial wavefunctions of both FL, composite FL and spinon FS states [70–73] suggest that they all obey the $L_M \log L_M$ scaling. We calculate S_2 utilizing Eq. (22) via joint distributions. In Fig. 6(a), the solid line is the exact formula for Rényi entropy at the non-interacting limit $h \rightarrow \infty$, and the dots are numerically measured S_2 in the paramagnetic phase $h = 6.0$ and at the QCP $h = h_c = 3.27$. Naively, this figure seems to indicate that the value of S_2 is independent of h in the entire paramagnetic phase and at the QCP. However, as will be shown below, more careful analysis indicates the opposite conclusion.

Before we discuss a more careful analysis in the next section, let us conclude this section by providing a quick summary of Figs. 5 and 6. Using DQMC simulations, we find that the spin disorder operator is very sensitive to this itinerant Ising QCP, and exhibits a diverging peak, because it coincides with the order parameter of this QCP and thus direct probe the diverging critical fluctuations. As for the charge disorder operator and S_2 , they seem to behave as the non-interacting limit. If this conclusion is true, it implies that the exact relation of the non-interacting limit, $S_2 = -2 \log |X_M^\rho(\frac{\pi}{2})|$, should survive in the FL. Because measuring $|X_M^\rho(\frac{\pi}{2})|$ costs much less numerical resource with much better data quality (equal time measurement without replicas) than S_2 , this observation seems to provide a much more efficient methods to probe S_2 in FLs and nFLs (near QCPs). However, as will be shown in the next section, more careful analysis indicates that $|X_M^\rho(\frac{\pi}{2})|$ and S_2 are clearly distinct in interacting systems. The difference between them is small (but nonzero) in the FL phase, and becomes much more severe as we approach the QCP and the nFL phase.

D. Scaling analysis for EE and disorder operators at QCP

To examine the interaction dependence of S_2 and X_M^ρ , we create 50×50 QMC auxiliary-field configurations to imitate the joint distribution of $\{s, s'\}$. For each pair of auxiliary-field configuration, we calculate $EE_{M,ss'} = \det[G_{M,s}G_{M,s'} + (\mathbb{1} - G_{M,s})(\mathbb{1} - G_{M,s'})]$ and $X_{M,ss'}^\rho = \det[G_{M,s}G_{M,s'} + (\mathbb{1} - G_{M,s})(\mathbb{1} - G_{M,s'}) + i(G_{M,s} - G_{M,s'})]$ and plot their distributions in Fig. 6(b). Here we set $h = h_c = 3.27$ and 10 independent Markov chains are used to yield the errorbar of each $EE_{M,ss'}$ and $X_{M,ss'}^\rho$ data points. As shown in Eqs. (21) and (22), the mean values of $EE_{M,ss'}$ and $X_{M,ss'}^\rho$, after average over all joint auxiliary-field configurations, are e^{S_2} and $X_M^\rho(\frac{\pi}{2})$ re-

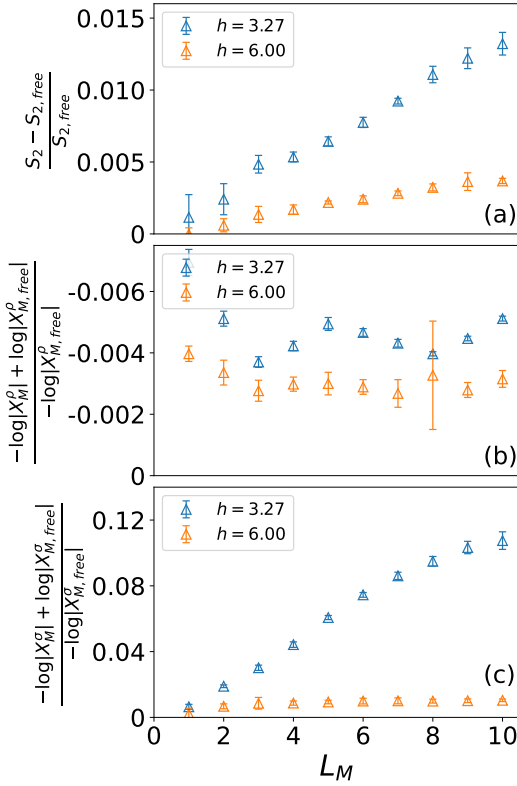


FIG. 7. (a,b,c) Deviation from the non-interacting limit in the FL phase $h = 6.00$ and at the QCP $h = 3.27$ for (a) S_2 (b) $-2 \log |X_M^\rho(\frac{\pi}{2})|$ and (c) $-2 \log |X_M^\sigma(\pi)|$. Within the system sizes that we can access, these deviations does not decrease with system size. Instead, the deviation of S_2 and $-2 \log |X_M^\sigma(\pi)|$ show clear increase, indicating that it is not due to finite-size effects.

spectively.

The logarithms of the two average values are marked in Fig. 6(b) as the orange and blue vertical lines, respectively, while the red vertical line marks the free-fermion value of $S_2 = -2 \log |X_M^\rho(\frac{\pi}{2})|$ at the $h \rightarrow \infty$ limit. By comparing the three vertical lines in Fig. 6(b), we find that at the QCP, S_2 no longer coincides with $-2 \log |X_M^\rho(\frac{\pi}{2})|$. In comparison with non-interacting fermions, interactions increase the value of S_2 but reduces the value of $-2 \log |X_M^\rho(\frac{\pi}{2})|$. Although the deviation from the free-fermion value is small ($< 2\%$), the distribution shown in Fig. 6(b) clearly indicate that this deviation is beyond the error bar.

More importantly, this deviation from the free-fermion limit is not due to finite-size effects, because it increases as the system size increases towards the thermal dynamic limit, as shown in Fig. 7(a) and (b). For Rényi entropy S_2 , Fig. 7(a) shows that away from the QCP ($h = 6$), deviations from the free-fermion value increases with L_M , but the increase seems to saturate when L_M approaches 12. This saturation behavior suggests that in a FL, S_2 has the same scaling form as non-interacting systems, $S_2 \sim s_{2d} L_M \log L_M$, but the coefficient of s_{2d} gradually increases as interactions are turned on. In contrast to the free fermion limit, where s_{2d} only depends on the shapes of the FS and M , its value is sensitive to the inter-

action strength in a FL. At the QCP ($h = 3.27$), the deviation of S_2 from the free-fermion limit increases much faster than the FL phase [Fig. 7(a)], and up to the largest system size that we can access $L_M = 12$ and $L = 24$, a saturation is not clearly observed. This increasing trend indicates three possible scenarios. (1) If the increase never saturates at large L_M , it would indicate that S_2 at the QCP follows a different scaling form, which increases faster than $L_M \log L_M$, e.g., L_M^α with a power between 1 and 2 or $L_M (\log L_M)^\alpha$ with $\alpha > 1$. (2) If the increase eventually saturates at large L_M , it would indicate that S_2 still follows the functional form of $L_M \log L_M$, but with a coefficient much larger than free-fermions ($h \rightarrow \infty$) or the FL phase ($h = 6$). (3) In the third scenario, the deviation eventually starts to decrease at some large L_M . If it decrease back to zero at the thermodynamic limit ($L_M \rightarrow \infty$), it would imply that interactions and QCPs have no impact on S_2 , whose value remains identical to the free theory. Although this third scenario is in principle possible, to the largest system size that we can access, we don't observe any signature for this deviation to start decreasing at large L_M , and thus no evidence supports it. For both scenarios (1) and (2), critical fluctuations near the QCP have a nontrivial impact on S_2 , i.e., S_2 is sensitive to the presence of an itinerant QCP.

For the charge disorder operator $X_M^\rho(\frac{\pi}{2})$, we find from in Fig. 7(b) that the deviation from the free fermion limit seems to saturate at large L_M , indicating that $X_M^\rho(\frac{\pi}{2})$ maintains its functional form $\sim L_M \log L_M$ in the FL and nFL phases, and the deviation only modifies that coefficient of this $L_M \log L_M$ term. This deviation seems to increase a bit as we approach the QCP ($h = 3.27$), in comparison with the FL phase $h = 6.00$. However, this increase is much weaker than the increase of the deviation of S_2 at the QCP, indicating that the charge disorder operator is much less sensitive to the itinerant QCP than S_2 .

For comparison, we also plot the deviation for the spin disorder operator from the free fermion limit in Fig. 7(c). Away from the QCP, the deviation seems to saturate. At the QCP, the deviation increases dramatically, indicating that the spin disorder operator is very sensitive to the quantum phase transition. This observation is consistent with the diverging spin fluctuations discussed in the previous section. Similar with the S_2 case, whether the $L_M \log L_M$ scaling form will change, or, there is a large coefficient at the QCP, are beyond our current system sizes.

In summary, we find that although the values of S_2 and $-2 \log |X_M^\rho(\frac{\pi}{2})|$ seems to be close to the free fermion limit, interactions push their values towards different directions, increasing S_2 and decreasing $-2 \log |X_M^\rho(\frac{\pi}{2})|$. These two opposite trends are beyond the numerical error bar, and the effects becomes stronger as the system size increases, indicating that it is not due to the finite-size effect. In the FL phase away from the QCP, the difference between S_2 and $-2 \log |X_M^\rho(\frac{\pi}{2})|$ are small, but it become more much severe at the QCP. The spin disorder operator, $-2 \log |X_M^\sigma(\pi)|$, on the other hand, does exhibit enhanced signal at the QCP.

VI. DISCUSSIONS

Accessing entanglement measures in interacting fermion systems has been a long standing problem. Early attempts that do not require replicas [12, 13] are often plagued by large fluctuations. Implementing replicas [14, 74] allows one to circumvent these issues but are numerically demanding. The same holds for the entanglement spectra and Hamiltonian [15]. In this work, we investigate an alternative, namely, the fermion disorder operator which provides similar entanglement information. From the technical point of view, this quantity does not rely on replicas and can be computed on the fly in an auxiliary field QMC simulation.

Generically, the disorder operator and Rényi EEs are different quantities. In particular, the disorder operator is formulated in terms of a global symmetry of the model system, whereas the Rényi entropies are defined without any symmetry considerations. At small angles, the disorder operator relates to so called bi-partite fluctuations that have been introduced as an entanglement witness [11]. Despite the obvious differences, for non-interacting Fermion systems, there is a one-to-one mapping between the *charge* disorder operator at a given angle, and the Rényi entropies. As such, for a bipartition of space with L_M^d the volume of one partition, we observe a $L_M^{d-1} \log L_M$ law for the FL for both quantities.

Beyond the non-interacting limit, notable differences appear. For the one-dimensional case with spin and charge degrees of freedom, the prefactor of the $\log L_M$ law for the spin and charge disorder operators captures the Luttinger parameter in the respective sectors. This contrasts with the Rényi entropy that picks up the central charge. In fact, we show that the disorder operator offers a much better estimation of the Luttinger parameter (the coefficient in the $\log L$ scaling) as compared to the traditional fitting from the structure factors.

To investigate the nature of the disorder operator in two-dimensions, we concentrate on metallic Ising ferromagnetic quantum criticality [34, 36]. *Deep* in the ordered and disordered FLs phases, the spin and charge disorder operators show very similar behaviors and follow a $L_M \log L_M$ law with prefactor dictated by the FS topology. In the proximity of the phase transition we observe marked differences between both symmetry sectors. In fact, in this special case, the generator of the U(1) spin symmetry corresponds to the order parameter and the spin-disorder operator shows singular behavior at criticality. On the other hand, the charge disorder operator does not pick up the phase transition and smoothly interpolates between the order and disordered FL phases. Remarkably, and on the considered lattice sizes, the scaling of the spin disorder operator at criticality reflects that of the Rényi entropy, and supports the interpretation of either a deviation from the $L_M \log L_M$ law, or, greatly enhanced coefficient of the scaling form. Our examples in one and two dimensions, illustrate the symmetry dependence in the design and interpretation of the disorder operator.

A key point in considering the disorder operator is that it seems possible to access experimentally. As mentioned previously, at small angles, it maps onto two-point correlation functions of local operators. Such quantities are routinely com-

puted in scattering experiments. For example neutron scattering experiments provides the the dynamical spin structure factor, from which equal time correlation functions can be extracted. With this in mind, understanding the intricacies of the disorder operator and what we can learn from it for various phases of correlated quantum matter and across various QCPs becomes more pressing. We foresee a number of future investigations with disorder operator that include, on-going experiments in quantum switch device and optical lattices [75–77], lattice models for quantum critical metals [78, 79], correlated insulators and superconductors in moiré lattice models [80–84], exotic states of matter such as deconfined quantum criticality, emergent quantum spin liquids and topological fermionic states [85–94].

ACKNOWLEDGEMENT

W.L.J., B.-B.C. and Z.Y.M. would like to thank Zheng Yan for insightful discussions on the EE and ES, acknowledge support from the Research Grants Council of Hong Kong SAR of China (Grant Nos. 17303019, 17301420, 17301721, AoE/P-701/20 and 17309822), the GD-NSF (no.2022A1515011007), the Strategic Priority Research Program of the Chinese Academy of Sciences (Grant No. XDB33000000), the K. C. Wong Education Foundation (Grant No. GJTD-2020-01) and the Seed Funding "Quantum-Inspired explainable-AI" at the HKU-TCL Joint Research Centre for Artificial Intelligence. M.C. acknowledges support from NSF under award number DMR-1846109. We thank the HPC2021 platform under the Information Technology Services at the University of Hong Kong, and the Tianhe-II platform at the National Supercomputer Center in Guangzhou for their technical support and generous allocation of CPU time. F.F.A. and Z.L. thank Cenke Xu and Chaoming Jian for discussion on the relation of the disorder operator and Rényi entropies for free electrons. F.F.A. acknowledges support from the DFG funded SFB 1170 on Topological and Correlated Electronics at Surfaces and Interfaces. Z.L. thanks the Würzburg-Dresden Cluster of Excellence on Complexity and Topology in Quantum Matter ct.qmat (EXC 2147, project-id 390858490) for financial support.

VII. SUPPLEMENTAL MATERIALS FOR

FERMION DISORDER OPERATOR: THE HEDGEHOG AND THE FOX OF QUANTUM MANY-BODY ENTANGLEMENT

A. Section I: Disorder operator in QMC calculation

1. Disorder operator in charge channel

We explain the implementation of disorder operator in the determinant QMC. We first consider the disorder operator in charge channel, $\hat{X}_M^\rho(\theta) = \prod_{i \in M} e^{i\hat{n}_i \theta}$. For convenience, we denote $X_M^\rho = \langle \hat{X}_M^\rho(\theta) \rangle$. Below, we show that in QMC simulation, the expectation value of the disorder operator is an equal-time measurement of fermion Green's function.

Define the fermion Green's function matrix of certain configuration, $G_{s,i\sigma,j\sigma'} = \langle \hat{c}_{i\sigma} \hat{c}_{j\sigma'}^\dagger \rangle_s$. i, j labels the lattice site, and s labels the configuration. One has,

$$X_M^\rho = \sum_s P_s \frac{\text{Tr}[\hat{U}_s(\beta, \tau) \prod_{i \in M} e^{i\hat{n}_i \theta} \hat{U}_s(\tau, 0)]}{\text{Tr}[\hat{U}_s(\beta, 0)]} \quad (35)$$

where $P_s = \frac{\text{Tr}[\hat{U}_s(\beta, 0)]}{\sum_s \text{Tr}[\hat{U}_s(\beta, 0)]}$ is the normalized weight of each configuration. We define $N_M(N_{M,\sigma})$ to be the number of sites(spin flavor) of whole system, N_σ is the number of spin flavors. The total Hamiltonian \hat{H} can be expressed in site and spin basis, and constructed as a matrix H with dimension $N_\sigma N \times N_\sigma N$. Applying the expression $\text{Tr}[e^{\hat{H}}] = \text{Det}[1 + e^H]$, and $\text{Det}[1 + AB] = \text{Det}[1 + BA]$,

$$\begin{aligned} X_M^\rho &= \sum_s P_s \frac{\text{Det}[1 + B_s(\beta, \tau) e^{T^\rho} B_s(\tau, 0)]}{\text{Det}[1 + B_s(\beta, 0)]} \\ &= \sum_s P_s \frac{\text{Det}[1 + B_s(\tau, 0) B_s(\beta, \tau) e^{T^\rho}]}{\text{Det}[1 + B_s(\tau, 0) B_s(\beta, \tau)]} \\ &= \sum_s P_s \frac{\text{Det}[1 + (G_s^{-1} - 1) e^{T^\rho}]}{\text{Det}[G_s^{-1}]} \\ &= \sum_s P_s \text{Det}[G_s + (1 - G_s) e^{T^\rho}] \\ &= \sum_s P_s X_{M,s}^\rho \end{aligned} \quad (36)$$

T^ρ is the $N_\sigma N \times N_\sigma N$ diagonal matrix with $T_{i\sigma,i\sigma}^\rho = \begin{cases} i\theta, & i \in M \\ 0, & i \notin M \end{cases}$.

We first swap the index of G to separate the sites in M , and out of M , which does not change the determinant. We denote N_M as the number of sites in region M and site $i \in M$, $j \notin M$. Then the diagonal element of e^T transfers to $[\underbrace{e^{i\theta}, \dots, e^{i\theta}}_{N_\sigma N_M}, \underbrace{1, \dots, 1}_{N_\sigma (N - N_M)}]$. Then, we have

$$\begin{aligned} X_{M,s}^\rho &= \text{Det} \left[\begin{pmatrix} G_{ii} & \dots & G_{ij} \\ \vdots & \ddots & \vdots \\ G_{ji} & \dots & G_{jj} \end{pmatrix}_{M,s} + \begin{pmatrix} 1 - G_{ii} & \dots & -G_{ij} \\ \vdots & \ddots & \vdots \\ -G_{ji} & \dots & 1 - G_{jj} \end{pmatrix}_{M,s} \begin{pmatrix} e^{i\theta} & \dots & 0 \\ \vdots & \ddots & \vdots \\ 0 & \dots & 1 \end{pmatrix} \right] \\ &= \text{Det} \left[\begin{pmatrix} G_{ii} & \dots & G_{ij} \\ \vdots & \ddots & \vdots \\ G_{ji} & \dots & G_{jj} \end{pmatrix}_{M,s} + \begin{pmatrix} (1 - G_{ii})e^{i\theta} & \dots & -G_{ij} \\ \vdots & \ddots & \vdots \\ -G_{ji}e^{i\theta} & \dots & 1 - G_{jj} \end{pmatrix}_{M,s} \right] \\ &= \text{Det} \left[\begin{pmatrix} G_{ii} + (1 - G_{ii})e^{i\theta} & \dots & 0 \\ \vdots & \ddots & \vdots \\ G_{ji}(1 - e^{i\theta}) & \dots & 1 \end{pmatrix}_{M,s} \right] \\ &= \text{Det} [e^{i\theta} \mathbb{1} + (1 - e^{i\theta}) G_{M,s}] \end{aligned} \quad (37)$$

where $G_{M,s}$ represents the Green's function matrix projection on M with $N_\sigma N_M \times N_\sigma N_M$ dimension, i.e., $G_{M,s,i\sigma,j\sigma'} = G_{s,i\sigma,j\sigma'}$ for $i, j \in M$.

Furthermore, if s_z is the conserved quantity, i.e. G_M is block-diagonal and $G_{s,i\sigma,j\sigma'} \propto \delta_{\sigma\sigma'}$. Here, $X_{M,\sigma,s}$ denotes the projection of $X_{M,s}$ on the spin basis σ . And Eq. (37) simplifies to,

$$\begin{aligned} X_{M,s}^\rho &= \prod_\sigma \text{Det} [e^{i\theta} + (\mathbb{1} - e^{i\theta})G_{M,\sigma,s}] \\ &= \prod_\sigma X_{M,\sigma,s}^\rho \end{aligned} \quad (38)$$

2. Disorder operator in spin channel

Likewise in above subsection, we consider the disorder operator in spin channel, $\hat{X}_M^\sigma(\theta) = \prod_{i \in M} e^{i\hat{S}_i^z\theta}$ where $\hat{S}_i^z = \frac{1}{2}(\hat{n}_{i\uparrow} - \hat{n}_{i\downarrow})$ is the z -direction spin operator for fermion at lattice site i , and use $X_M^\sigma = \langle \hat{X}_M^\sigma(\theta) \rangle$. The difference between the disorder operator of spin and charge channel comes from the matrix T , where $T_{i\sigma,i\sigma}^\sigma = \frac{i\theta}{2}$ when $i \in M, \sigma = \uparrow$, $T_{i\sigma,i\sigma}^\sigma = \frac{-i\theta}{2}$ when $i \in M, \sigma = \downarrow$ and $T_{i\sigma,i\sigma}^\sigma = 0$ for $i \notin M$.

Utilizing the same derivation as above and given s_z is the conserved quantity, eventually we have,

$$\begin{aligned} X_{M,s}^\sigma &= \text{Det} [e^{\frac{i\theta}{2}} + (\mathbb{1} - e^{\frac{i\theta}{2}})G_{M,\uparrow,s}] \times \text{Det} [e^{\frac{-i\theta}{2}} + (\mathbb{1} - e^{\frac{-i\theta}{2}})G_{M,\downarrow,s}] \\ &= X_{M,\uparrow,s}^\sigma X_{M,\downarrow,s}^\sigma \end{aligned} \quad (39)$$

We notice that the relation between two channels for certain auxiliary field s , $X_{M,\uparrow,s}^\rho(\theta) = X_{M,\uparrow,s}^\sigma(2\theta)$ and $= X_{M,\downarrow,s}^\rho(\theta) = X_{M,\downarrow,s}^{\sigma,*}(2\theta)$. If Z_2 symmetry of inverted spin is not broken, e.g. the disorder phase of Fig. 3(c) in the main text, one additionally has $X_{M,\uparrow,s}^\rho(\theta) = X_{M,\downarrow,s}^\rho(\theta)$. Following, we denote $X_{M,\sigma,s}(\theta) = \text{Det} [e^{i\theta} + (1 - e^{i\theta})G_{M,\sigma,s,ii}]$ to simplify the derivation.

B. Section II: Disorder operator at various angle

1. Small angle expansion

First, we derive the small angle expansion of the disorder operator in continuum limit as a general consideration. Take charge channel as the example,

$$\begin{aligned} -\log |X_M^\rho| &= -\log \left| \left\langle e^{i\theta \hat{N}_M} \right\rangle \right| \\ &= -\log \left| 1 + i\theta \left\langle \hat{N}_M \right\rangle - \frac{\theta^2}{2} \left\langle \hat{N}_M^2 \right\rangle + O(\theta^2) \right| \\ &= -\log \sqrt{\left(1 - \frac{\theta^2}{2} \left\langle \hat{N}_M^2 \right\rangle \right)^2 + \theta^2 \left\langle \hat{N}_M \right\rangle^2 + O(\theta^2)} \\ &= -\log \sqrt{1 - \theta^2 (\langle \hat{N}_M^2 \rangle - \langle \hat{N}_M \rangle^2) + O(\theta^2)} \\ &= \frac{\theta^2}{2} (\langle \hat{N}_M^2 \rangle - \langle \hat{N}_M \rangle^2) + O(\theta^2) \end{aligned} \quad (40)$$

We find the leading order is of θ^2 , where the coefficient is the known as the density fluctuations [22, 25], and also has the same definition of the cumulant C_M^2 .

To further apply Eq. (40) on the lattice, we start from free fermion where there is no auxiliary field s to sample and the P_s reduces to identity matrix.

$$-\log |X_M^\rho| = -\log \left| \sum_s P_s \prod_\sigma X_{M,\sigma,s}^\rho \right| = -\sum_\sigma \log |X_{M,\sigma}^\rho| \quad (41)$$

Notice that diagonal matrix element of X_M^ρ is of order $O(1)$, while for off-diagonal matrix element is of $O(\theta)$. We expand

the determinant to $O(\theta^2)$ term,

$$\begin{aligned}
X_{M,\sigma}^\rho &= \prod_i (e^{i\theta} + (1 - e^{i\theta})G_{M,\sigma,ii}) - \sum_{\{i,j\}} \frac{(1 - e^{i\theta})^2}{2} G_{M,\sigma,ij}G_{M,ji} + O(\theta^2) \\
&= \prod_i \left(1 + i\theta - \frac{\theta^2}{2} + (-i\theta + \frac{\theta^2}{2})G_{M,\sigma,ii} \right) + \sum_{\{i,j\}} \frac{\theta^2}{2} G_{M,\sigma,ij}G_{M,ji} + O(\theta^2) \\
&= 1 + i\theta \sum_i (1 - G_{M,\sigma,ii}) - \frac{\theta^2}{2} \sum_i (1 - G_{M,\sigma,ii}) - \frac{\theta^2}{2} \sum_{\{i,j\}} (1 - G_{M,\sigma,ii})(1 - G_{M,\sigma,ji}) - \frac{\theta^2}{2} C_{M,\sigma}^{2,latt} + O(\theta^2)
\end{aligned} \tag{42}$$

where $\{i, j\}$ denotes all different combinations for $i, j \in M$ with $i \neq j$. We define,

$$C_{M,\sigma}^{2,latt} \equiv - \sum_{\{i,j\}} G_{M,\sigma,ij}G_{M,ji} = \sum_{\{i,j\}} (\langle \hat{n}_i \hat{n}_j \rangle - \langle \hat{n}_i \rangle \langle \hat{n}_j \rangle) \equiv \sum_{\{i,j\}} C_{ij} \tag{43}$$

Above, we utilize the Wick theorem. The definition of $C_{M,\sigma}^{2,latt}$ is density fluctuations (or the cumulant) defined on the lattice. Furthermore, in the single sublattice model, due to the translation symmetry, $G_{M,\sigma,ii} = 1 - n_\sigma$ is identical for all sites, we do further simplification on Eq. (43),

$$\begin{aligned}
-\log|X_M^\rho| &= - \sum_\sigma \log \left| 1 - \frac{\theta^2}{2} \sum_i (1 - G_{M,\sigma,ii}) - \frac{\theta^2}{2} \sum_{\{i,j\}} (1 - G_{M,\sigma,ii})(1 - G_{M,\sigma,ji}) \right. \\
&\quad \left. - \frac{\theta^2}{2} C_{M,\sigma}^{2,latt} + i\theta \sum_i (1 - G_{M,\sigma,ii}) + O(\theta^2) \right| \\
&= - \sum_\sigma \log \sqrt{\left(1 - \frac{\theta^2}{2} n_\sigma N_M - \frac{\theta^2}{2} n_\sigma^2 N_M (N_M - 1) - \frac{\theta^2}{2} C_{M,\sigma}^{2,latt} \right)^2 + (\theta n_\sigma N_M)^2 + O(\theta^2)} \\
&= - \sum_\sigma \log \sqrt{1 - \theta^2 (n_\sigma N_M + n_\sigma^2 N_M (N_M - 1) + C_{M,\sigma}^{2,latt}) + \theta^2 n_\sigma^2 N_M^2 + O(\theta^2)} \\
&= - \sum_\sigma \log \sqrt{1 - \theta^2 (n_\sigma N_M - n_\sigma^2 N_M + C_{M,\sigma}^{2,latt}) + O(\theta^2)} \\
&= \frac{\theta^2}{2} \sum_\sigma \left(N_M (n_\sigma - n_\sigma^2) + C_{M,\sigma}^{2,latt} \right) + O(\theta^2)
\end{aligned} \tag{44}$$

Note N_M in Eq. (44) is the number of site of region M , and \hat{N}_M in Eq. (40) is the total particle number operator of region M . Without $C_{M,\sigma}^{2,latt}$, the disorder operator behaves as the volume law for any system. In addition, if $C_{M,\sigma}^{2,latt}$ is strictly zero at $r > r_0$, the behavior of is still volume law plus a constant at $r > r_0$. Generally speaking, various function form of disorder operator is determined by the function form of C_{ij} and the shape of region M .

Compare Eq. (44) with Eq. (40), the two terms $N_M(n_\sigma - n_\sigma^2)$, $C_{M,\sigma}^{2,latt}$ in Eq. (44) correspond $r = 0$ and $r \neq 0$ part of density fluctuations C^2 in Eq. (40), respectively, since the summation for the latter requires $i \neq j$. Here we use $\hat{n}_i^2 = \hat{n}_i$ for the properties of fermionic particle density operator. As a consequence, we expect $C_{M,\sigma}^{2,latt} \approx C_{M,\sigma}^2$ at thermodynamic limit. Finally, we conclude the small θ expansion of the disorder operator describes the performance of two points correlation function.

2. large angle at $\theta = \pi/2$ and $2\pi/3$

In non-interacting case, taking $\theta = \frac{\pi}{2}$ in X_M^ρ and omit σ index, we have,

$$X_M^\rho \left(\frac{\pi}{2} \right) = \det [G_M + i(\mathbb{1} - G_M)] \tag{45}$$

We display the exact relation of Eq.(8) and (9) in the main text,

$$\begin{aligned}
S_2 &= -\log\{\det[G_M^2 + (\mathbb{1} - G_M)^2]\} \\
&= -\log\{\det[G_M + i(\mathbb{1} - G_M)] \times \det[G_M - i(\mathbb{1} - G_M)]\} \\
&= -\log\{X_M(\frac{\pi}{2})X_M(\frac{\pi}{2})^*\} \\
&= -\log|X_M(\frac{\pi}{2})|^2 \\
&= -2\log|X_M(\frac{\pi}{2})|.
\end{aligned} \tag{46}$$

And for $\theta = \frac{2\pi}{3}$,

$$\begin{aligned}
S_3 &= -\frac{1}{2}\log\{\det[G_M^3 + (\mathbb{1} - G_M)^3]\} \\
&= -\frac{1}{2}\log\{\det[\mathbb{1} - 3G_M + G_M^2]\} \\
&= -\frac{1}{2}\log\{\det\left[\frac{1}{4}(\mathbb{1} - 3G_M)^2 + \frac{3}{4}(\mathbb{1} - G_M)^2\right]\} \\
&= -\frac{1}{2}\log\{\det\left[\frac{1}{2}(\mathbb{1} - 3G_M) + i\frac{\sqrt{3}}{2}(1 - G_M)\right] \times \left[\frac{1}{2}(\mathbb{1} - 3G_M) - i\frac{\sqrt{3}}{2}(1 - G_M)\right]\} \\
&= -\frac{1}{2}\log\{X_M(\frac{2\pi}{3})X_M(\frac{2\pi}{3})^*\} \\
&= -\frac{1}{2}\log|X_M(\frac{2\pi}{3})|^2 \\
&= -\log|X_M(\frac{2\pi}{3})|.
\end{aligned} \tag{47}$$

3. $\theta = \pi$

We emphasize that, in contrast with the bosonic system, the disorder operator defined in this form is differ from the entanglement entropy in the free system by taking $\theta = \pi$ in Ref. [22]. As shown above, one can strictly prove the equality between and the 2nd Rényi entropy between the disorder operator at $\frac{\pi}{2}$. For free fermion case, by taking $\theta = \pi$ in X_M^ρ , one obtain,

$$-\log|X_M^\rho(\pi)| = -\log\det[-1 + 2G_M], \tag{48}$$

which gives divergence since the eigenvalue of G_M has value of 0.5.

C. Section III: Density correlation function and disorder operator of several free fermionic system

We derive the density correlation function $C(\mathbf{r}) = C_{ij}$, $r \neq 0$ at zero temperature analytically in several free 1D and 2D models with translation symmetry. Here \mathbf{i}, \mathbf{j} represent lattice site, $\mathbf{r} = \mathbf{i} - \mathbf{j}$, and $r = |\mathbf{r}|$. We set the length of unit cell in both 1d chain and 2d square lattice to be 1. We also calculate the density fluctuations C^2 in the region M by the integral, which is the coefficient before small θ expansion. The shape of M is chosen as Fig. 3(b) and (d) in the main text.

1. Ground state of 1D fermions with FS

We use Hamiltonian Eq.(11) in the main text,

$$\hat{H} = t_1 \sum_{\langle i,j \rangle} \hat{c}_i^\dagger \hat{c}_j + t_2 \sum_{\langle\langle i,j \rangle\rangle} \hat{c}_i^\dagger \hat{c}_j + \mu \sum_i \hat{n}_i \tag{49}$$

The density correlation function only depend on k_F ,

$$C(r) = \frac{g(-1 + \cos(2k_F r))}{2\pi^2 r^2} \tag{50}$$

where g is fermion species. We find $C(r) \approx \frac{1}{r^2}$, and the global coefficient $(-1 + \cos(2k_F r))$ is related to k_F , which we identified as the oscillation term. We derivate the density fluctuation as following,

$$C^2 = \frac{g}{\pi^2} \log L_M + o(1). \quad (51)$$

Comparing Eqs. (50) and (51), the oscillation term do not effect the coefficient of leading term. And $\log L$ comes from $\frac{1}{r^2}$ relation for 1D.

2. Ground state of 1D gapped fermionic system

We use Hamiltonian as Eq. (49) added a staggered chemical potential, and written,

$$\hat{H} = t_1 \sum_{\langle i,j \rangle} \hat{c}_i^\dagger \hat{c}_j + t_2 \sum_{\langle\langle i,j \rangle\rangle} \hat{c}_i^\dagger \hat{c}_j + \Delta \sum_i (-1)^i \hat{c}_i^\dagger \hat{c}_i \quad (52)$$

Generally, the system consists of two sublattice. The density correlation at large distance writes,

$$C(r) \sim e^{-f(\Delta)r}, r \gg 1. \quad (53)$$

$f(\Delta)$ is a function of gap Δ . The gapped physics drives the density fluctuation to converge to a constant at large scale,

$$C^2 = o(1), L_M \gg 1. \quad (54)$$

3. Finite temperature of 1D fermionic system with fermi surface

We still use Hamiltonian as Eq. (49), and study the density correlation at finite temperature, one have

$$C(r) \sim e^{-\xi r} (-1 + 2 \cos(k_F r)), \quad (55)$$

where ξ denotes the thermodynamics correlation length. Since exponential decay is convergent by the integral, the disorder operator is given as the volume law,

$$C^2 = L_M + o(1). \quad (56)$$

4. Ground state of 2D fermions with FS

Next, we study a 2D free fermion system, generated by the Hamiltonian Eq. (13) in the main text.

$$\hat{H} = t_1 \sum_{\langle i,j \rangle} \hat{c}_i^\dagger \hat{c}_j + t_2 \sum_{\langle\langle i,j \rangle\rangle} \hat{c}_i^\dagger \hat{c}_j + \mu \sum_i \hat{n}_i. \quad (57)$$

We discuss one simplest case, that is the circular FS, denoted by k_F . The density correlation function is only dependent on r . We have,

$$\begin{aligned} C(r) &= \frac{gk_F^2}{4\pi^2} \frac{J_1(k_F r)}{r^2} \\ &\approx \frac{gk_F}{4\pi^3 r^3} (1 - \sin(2k_F r)) \end{aligned} \quad (58)$$

J_1 represent the Bessel function. At large r , $C(r)$ obeys $\frac{1}{r^3}$ behavior with the oscillation coefficient. The leading term of the disorder operator has the well-known form $L_M^{d-1} \log L_M$, where d is the dimension,

$$C^2 = \frac{2k_F}{\pi^3} L_M \log L_M + o(L_M) \quad (59)$$

Unlike the 1D FS, the coefficient of leading term is related to k_F , which can be easily understand use the conjectures in Ref [30]. The result is one special case equation of Eq. (9) in the main text. Since we fixed the region M (FS) to be the square (circle), the double integral term is proportion to k_F . For general shape of fermi surface, we conclude the disorder operator written in Eq. (9) in the main text.

D. Section IV: Fitting details and quantitative estimation in 2d free systems

In the main text, we discussed 1d and 2d free fermions with FS, where in 1d, we use the conformal distance \tilde{L}_M to fit the Luttinger parameter. As the system size gets larger, the maximum of \tilde{L}_M increase, and the Luttinger parameter fitted by the large \tilde{L}_M gradually converge to the value of thermodynamic limit. Technically, one can push the system to large enough to get the accurate value. However, in 2d system, a good finite size modification parameter like \tilde{L}_M is hard to find, and there is not one simple method to judge the convergence to thermodynamic limit of fitting results. As we mentioned in Fig. 2 in the main text, we fit the function forms by certain fit range. Obviously, the choose of the fit range will change s a lot. Therefore, we first explore the effect by the fit range in 2d, and compare with the analytic value, obtained by Eq. (59). We define the lower(upper) boundary of fit range as $f_{low}(f_{up})$, and fit the raw data with the function form $-\log |X_M(\theta)| = s_{2d}(\theta)L_M \log L_M + bL_M + c$ in (a) and $-\log |X_M(\theta)|/L_M = s_{2d}(\theta) \log L_M + b$, using $L_M \in [f_{low}, f_{up}]$ in Fig. 8. And we use at least 5 data points to fit, i.e. $f_{up} \geq f_{low} + 5$. From this two panels in Fig. 8, one can see the different original data brings distinguishing s_{2d} , where we find (b) is more possible to get the accurate value. We conclude the general fit principle, that one would choose $f_{low} \gg 1$, and $f_{up} \ll L$ to avoid finite size effect. That requires large system size up to at least hundreds of L . Besides, we observe that (b) has wider fit range to get same close value of analytic results. Thus, one may use $-\log |X_M|/L_M$ versus $\log L_M$ to decrease finite size effect.

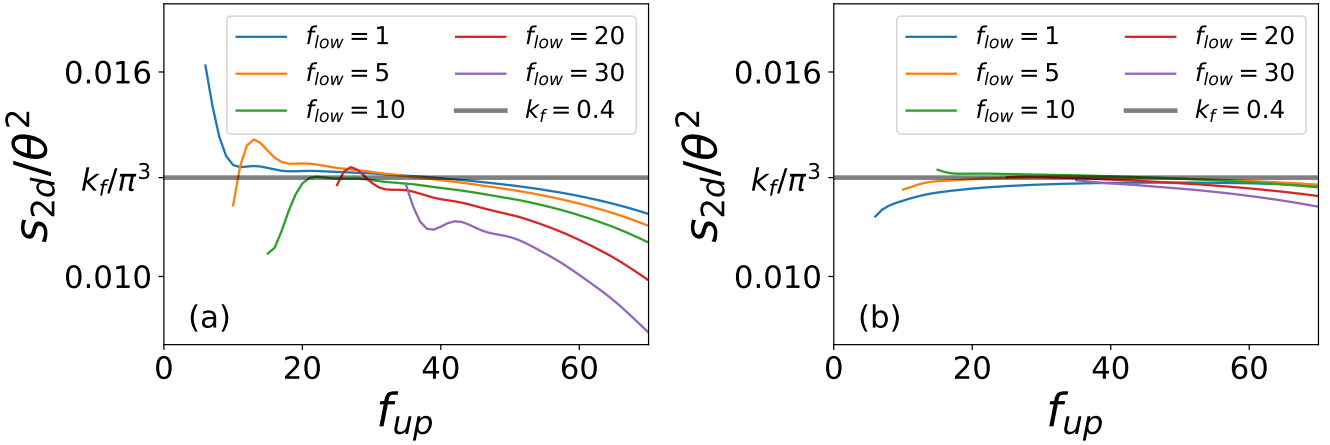


FIG. 8. Fit results with various fit range for free circular-shaped fermion at $L = 160$, $k_F = 0.4$. We choose few f_{low} shown by different color. The analytic value is given by Eq. (59) the black solid line. The original data is (a) $-\log |X_M|$ fitted by $s_{2d}(\theta)L_M \log L_M + bL_M + c$, adapted in Fig. 2(a) in the main text. (b) $-\log |X_M|/L_M$ versus $\log L_M$ fitted by the linear function $y = s_{2d}x + b$, adapted in Fig. 2(b) in the main text. For comparison, (b) has more similar values for same fit range compared with analytic value k_F/π^3 given by Eq. (59).

E. Section V: Traditional way to determine the Luttinger parameter in 1D

In this section, we briefly recapitulate basic results from the Tomonaga-Luttinger liquid theory [95–97], on the charge correlations which constitutes an prevailing way to extract the Luttinger charge exponent K_ρ numerically [50, 98, 99]. For the results listed below, we focus on the case with spin SU(2) symmetry and have the Luttinger parameter $K_\sigma = 1$ for the spin gapless states. In genenal, there exist multiple modes for the considered charge density correlation. Up to the first two dominant modes, we have

$$C(r) = -\frac{K_\rho}{(\pi r)^2} + A \frac{\cos(2k_F r)}{r^{1+K_\rho}} \ln^{-3/2}(r), \quad (60)$$

where A is a model-dependent parameters. The uniform mode (related to the r^{-2} term above) results in $S_\rho(k) \simeq K_\rho |k|/\pi$ for $k \rightarrow 0$, with $S_\rho(k) = 1/L \sum_{i,j} e^{-ikr_{ij}} C_{ij}$ the Fourier transformation of the charge correlation.

In practice, for the charge gapless phase like LL, the asymptotic behavior of $S_\rho(k)$ is *linear* with k as $k \rightarrow 0$, while in the charge-gapped phase we have $K_\rho = 0$ and the small- k *quadratic* scaling. This offers us a way of extracting K_ρ from charge density correlation. To be more specific, we employ a 2nd-order polynomial fitting $S_\rho(k) = A(k/\pi)^2 + B(k/\pi) + C$, from which the Luttinger charge exponent $K_\rho = B$.

The $S_\rho(k)$ results for $U = 2$ at the half-filling case of an $L = 256$ Hubbard chain with open boundary condition is shown in Fig. 9(a). Due to the exponentially small gap in the state, i.e., $\Delta_\rho \sim \exp(-t/U)$, in the small- k regime S_ρ show a slightly

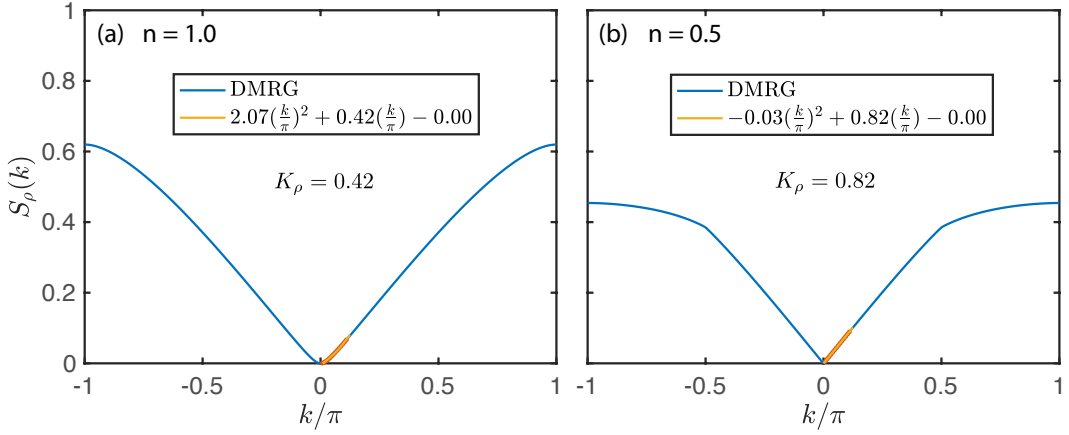


FIG. 9. In a $U = 2$, $L = 256$ Hubbard chain with open boundary condition, the charge structure factor S_ρ is shown versus k/π , for both (a) half-filling case $n = 1.0$ and (b) quarter-filling case $n = 0.5$. The blue solid lines are the DMRG calculated data with the red dot depicting the data used for the extrapolation. The yellow solid lines indicates the 2nd order extrapolation $S_\rho = A(\frac{k}{\pi})^2 + B(\frac{k}{\pi}) + C$, from which the Luttinger charge exponent can be extracted $K_\rho = B = 0.42$ for the half-filling case, and $K_\rho = 0.82$ for the quarter-filling case.

quadratic behavior, and from the small- k data (to eliminate the finite-size effect, here $k \in [2\pi/L, 2\pi n/L]$ with $n = 15$ chosen) we still get a finite value of $K_\rho = 0.42$ still far from the expected $K_\rho = 0$. For the quarter-filling case as shown in Fig. 9(b), the small- k data show clear linear behavior and we have $K_\rho = 0.82$ in great agreement with the value in the main text and also Bethe ansatz result [49]. As we have shown in the main text Fig.4, we find it is much easier to fit the charge disorder operator and extract its coefficient – the Luttinger parameter – from the $K_\rho \log L$ scaling with much less finite size effects.

[1] I. Berlin, The hedgehog and the fox: An essay on tolstoy's view of history, Weidenfeld & Nicolson (1953).

[2] J. L. Cardy and I. Peschel, Finite-size dependence of the free energy in two-dimensional critical systems, *Nuclear Physics B* **300**, 377 (1988).

[3] M. Srednicki, Entropy and area, *Phys Rev Lett* **71**, 666 (1993).

[4] C. Holzhey, F. Larsen, and F. Wilczek, Geometric and renormalized entropy in conformal field theory, *Nuclear Physics B* **424**, 443 (1994).

[5] P. Calabrese and J. Cardy, Entanglement entropy and quantum field theory, *Journal of Statistical Mechanics: Theory and Experiment* **2004**, P06002 (2004).

[6] E. Fradkin and J. E. Moore, Entanglement entropy of 2d conformal quantum critical points: Hearing the shape of a quantum drum, *Phys. Rev. Lett.* **97**, 050404 (2006).

[7] H. Casini and M. Huerta, Universal terms for the entanglement entropy in 2+1 dimensions, *Nucl. Phys. B* **764**, 183 (2007), arXiv:hep-th/0606256.

[8] A. Kitaev, Anyons in an exactly solved model and beyond, *Annals of Physics* **321**, 2 (2006).

[9] M. Levin and X.-G. Wen, Detecting topological order in a ground state wave function, *Phys. Rev. Lett.* **96**, 110405 (2006).

[10] H. Li and F. D. M. Haldane, Entanglement spectrum as a generalization of entanglement entropy: Identification of topological order in non-abelian fractional quantum hall effect states, *Phys. Rev. Lett.* **101**, 010504 (2008).

[11] H. F. Song, S. Rachel, C. Flindt, I. Klich, N. Laflorencie, and K. Le Hur, Bipartite fluctuations as a probe of many-body entanglement, *Phys. Rev. B* **85**, 035409 (2012).

[12] T. Grover, Entanglement of interacting fermions in quantum monte carlo calculations, *Phys Rev Lett* **111**, 130402 (2013).

[13] F. F. Assaad, T. C. Lang, and F. Parisen Toldin, Entanglement spectra of interacting fermions in quantum monte carlo simulations, *Phys. Rev. B* **89**, 125121 (2014).

[14] F. F. Assaad, Stable quantum monte carlo simulations for entanglement spectra of interacting fermions, *Physical Review B* **91**, 10.1103/PhysRevB.91.125146 (2015).

[15] F. Parisen Toldin and F. F. Assaad, Entanglement hamiltonian of interacting fermionic models, *Phys. Rev. Lett.* **121**, 200602 (2018).

[16] J. Zhao, Y.-C. Wang, Z. Yan, M. Cheng, and Z. Y. Meng, Scaling of entanglement entropy at deconfined quantum criticality, *Phys. Rev. Lett.* **128**, 010601 (2022).

[17] Z. Yan and Z. Y. Meng, Relating entanglement spectra and energy spectra via path-integral on replica manifold, arXiv e-prints , arXiv:2112.05886 (2021), arXiv:2112.05886 [cond-mat.str-el].

[18] J. Zhao, B.-B. Chen, Y.-C. Wang, Z. Yan, M. Cheng, and Z. Y. Meng, Measuring rényi entanglement entropy with high efficiency and precision in quantum monte carlo simulations, *npj Quantum Materials* **7**, 69 (2022).

[19] L. P. Kadanoff and H. Ceva, Determination of an operator algebra for the two-dimensional ising model, *Phys. Rev. B* **3**, 3918 (1971).

[20] E. Fradkin, Disorder operators and their descendants, *Journal of Statistical Physics* **167**, 427 (2017).

[21] J. Zhao, Z. Yan, M. Cheng, and Z. Y. Meng, Higher-form symmetry breaking at ising transitions, *Phys. Rev. Research* **3**,

033024 (2021).

[22] Y.-C. Wang, M. Cheng, and Z. Y. Meng, Scaling of the disorder operator at $(2+1)d$ u(1) quantum criticality, *Phys. Rev. B* **104**, L081109 (2021).

[23] X.-C. Wu, C.-M. Jian, and C. Xu, Universal Features of Higher-Form Symmetries at Phase Transitions, *SciPost Phys.* **11**, 33 (2021).

[24] X.-C. Wu, W. Ji, and C. Xu, Categorical symmetries at criticality, *Journal of Statistical Mechanics: Theory and Experiment* **2021**, 073101 (2021).

[25] Y.-C. Wang, M. Cheng, and Z. Y. Meng, *Scaling of the disorder operator at $(2+1)d$ u(1) quantum criticality* (2021).

[26] B.-B. Chen, H.-H. Tu, Z. Y. Meng, and M. Cheng, Topological disorder parameter: A many-body invariant to characterize gapped quantum phases, *Phys. Rev. B* **106**, 094415 (2022).

[27] M. B. Hastings, I. González, A. B. Kallin, and R. G. Melko, Measuring renyi entanglement entropy in quantum monte carlo simulations, *Physical Review Letters* **104**, 10.1103/PhysRevLett.104.157201 (2010).

[28] V. Alba, Out-of-equilibrium protocol for renyi entropies via the jarzynski equality, *Phys. Rev. E* **95**, 062132 (2017).

[29] J. D'Emidio, Entanglement entropy from nonequilibrium work, *Phys. Rev. Lett.* **124**, 110602 (2020).

[30] D. Gioev and I. Klich, Entanglement entropy of fermions in any dimension and the widom conjecture, *Phys Rev Lett* **96**, 100503 (2006).

[31] H. Leschke, A. V. Sobolev, and W. Spitzer, Scaling of renyi entanglement entropies of the free fermi-gas ground state: A rigorous proof, *Phys. Rev. Lett.* **112**, 160403 (2014).

[32] A. V. Sobolev, On the schatten-von neumann properties of some pseudo-differential operators, *Journal of Functional Analysis* **266**, 5886 (2014).

[33] A. V. Sobolev, Wiener-hopf operators in higher dimensions: The widom conjecture for piece-wise smooth domains, *Integral Equations and Operator Theory* **81**, 435 (2015).

[34] X. Y. Xu, K. Sun, Y. Schattner, E. Berg, and Z. Y. Meng, Non-fermi liquid at $(2+1)d$ ferromagnetic quantum critical point, *Phys. Rev. X* **7**, 031058 (2017).

[35] X. Y. Xu, Z. H. Liu, G. Pan, Y. Qi, K. Sun, and Z. Y. Meng, Revealing fermionic quantum criticality from new monte carlo techniques, *Journal of Physics: Condensed Matter* **31**, 463001 (2019).

[36] X. Y. Xu, A. Klein, K. Sun, A. V. Chubukov, and Z. Y. Meng, Identification of non-fermi liquid fermionic self-energy from quantum monte carlo data, *npj Quantum Materials* **5**, 65 (2020).

[37] X. Y. Xu, Quantum monte carlo study of strongly correlated electrons, *Acta Phys. Sin.* **71**, 127101 (2022).

[38] G. Pan, W. Jiang, and Z. Y. Meng, A sport and a pastime: Model design and computation in quantum many-body systems, *Chinese Physics B* **31**, 127101 (2022).

[39] The detailed DQMC implementation of the disorder operator, its relation with entanglement entropy at special angles in free system, the estimation of the difference between the disorder operator and the entanglement entropy in the interacting systems and the strong finite size effect in the estimating the Luttinger parameter 1D from the charge structure factor in the traditional DMRG analysis, are present in this Supplemental Material.

[40] P. Calabrese, M. Mintchev, and E. Vicari, Exact relations between particle fluctuations and entanglement in fermi gases, *EPL (Europhysics Letters)* **98**, 20003 (2012).

[41] L. S. Levitov and G. B. Lesovik, Charge distribution in quantum shot noise, *Jetp Letters* **58**, 230 (1993).

[42] I. Klich and L. Levitov, Quantum noise as an entanglement me-
ter, *Phys Rev Lett* **102**, 100502 (2009).

[43] H. F. Song, C. Flindt, S. Rachel, I. Klich, and K. Le Hur, Entanglement entropy from charge statistics: Exact relations for noninteracting many-body systems, *Physical Review B* **83**, 10.1103/PhysRevB.83.161408 (2011).

[44] I. Peschel, Calculation of reduced density matrices from correlation functions, *Journal of Physics A: Mathematical and General* **36**, L205 (2003).

[45] B. Swingle, Rényi entropy, mutual information, and fluctuation properties of fermi liquids, *Phys. Rev. B* **86**, 045109 (2012).

[46] H. Casini and M. Huerta, Entanglement entropy in free quantum field theory, *Journal of Physics A: Mathematical and Theoretical* **42**, 504007 (2009).

[47] T. Giamarchi and O. U. Press, *Quantum Physics in One Dimension*, International Series of Monographs on Physics (Clarendon Press, 2004).

[48] E. H. Lieb and F. Y. Wu, Absence of mott transition in an exact solution of the short-range, one-band model in one dimension, *Phys. Rev. Lett.* **20**, 1445 (1968).

[49] H. J. Schulz, Correlation exponents and the metal-insulator transition in the one-dimensional hubbard model, *Phys. Rev. Lett.* **64**, 2831 (1990).

[50] D.-W. Qu, B.-B. Chen, H.-C. Jiang, Y. Wang, and W. Li, Spin-triplet pairing induced by near-neighbor attraction in the cuprate chain, *arXiv e-prints*, arxiv: 2110.00564 (2021).

[51] Y. Liu, W. Jiang, A. Klein, Y. Wang, K. Sun, A. V. Chubukov, and Z. Y. Meng, Dynamical exponent of a quantum critical itinerant ferromagnet: A monte carlo study, *Phys. Rev. B* **105**, L041111 (2022).

[52] M. A. Metlitski and S. Sachdev, Quantum phase transitions of metals in two spatial dimensions. i. ising-nematic order, *Phys. Rev. B* **82**, 075127 (2010).

[53] W. Jiang, Y. Liu, A. Klein, Y. Wang, K. Sun, A. V. Chubukov, and Z. Y. Meng, Monte carlo study of the pseudogap and superconductivity emerging from quantum magnetic fluctuations, *Nature Communications* **13**, 2655 (2022).

[54] Z. H. Liu, G. Pan, X. Y. Xu, K. Sun, and Z. Y. Meng, Itinerant quantum critical point with fermion pockets and hotspots, *Proceedings of the National Academy of Sciences* **116**, 16760 (2019).

[55] A. Schlief, P. Lunts, and S.-S. Lee, Exact critical exponents for the antiferromagnetic quantum critical metal in two dimensions, *Phys. Rev. X* **7**, 021010 (2017).

[56] Z. H. Liu, X. Y. Xu, Y. Qi, K. Sun, and Z. Y. Meng, Itinerant quantum critical point with frustration and a non-fermi liquid, *Phys. Rev. B* **98**, 045116 (2018).

[57] Z. H. Liu, X. Y. Xu, Y. Qi, K. Sun, and Z. Y. Meng, Elective-momentum ultrasize quantum monte carlo method, *Physical Review B* **99**, 10.1103/PhysRevB.99.085114 (2019).

[58] M. A. Metlitski and S. Sachdev, Quantum phase transitions of metals in two spatial dimensions. ii. spin density wave order, *Phys. Rev. B* **82**, 075128 (2010).

[59] P. Lunts, M. S. Albergo, and M. Lindsey, Non-Hertz-Millis scaling of the antiferromagnetic quantum critical metal via scalable Hybrid Monte Carlo, *arXiv e-prints*, arXiv:2204.14241 (2022), arXiv:2204.14241 [cond-mat.str-el].

[60] M. H. Gerlach, Y. Schattner, E. Berg, and S. Trebst, Quantum critical properties of a metallic spin-density-wave transition, *Phys. Rev. B* **95**, 10.1103/PhysRevB.95.035124 (2017).

[61] Y. Schattner, M. H. Gerlach, S. Trebst, and E. Berg, Competing orders in a nearly antiferromagnetic metal, *Phys. Rev. Lett.* **117**, 097002 (2016).

[62] C. Bauer, Y. Schattner, S. Trebst, and E. Berg, Hierarchy of energy scales in an o(3) symmetric antiferromagnetic quantum

critical metal: A monte carlo study, *Physical Review Research* **2**, 10.1103/PhysRevResearch.2.023008 (2020).

[63] S. Lederer, Y. Schattner, E. Berg, and S. A. Kivelson, Enhancement of superconductivity near a nematic quantum critical point, *Phys. Rev. Lett.* **114**, 097001 (2015).

[64] L. Samuel, S. Yoni, B. Erez, and A. K. Steven, Superconductivity and non-fermi liquid behavior near a nematic quantum critical point, *Proc Natl Acad Sci U S A* **114**, E8798 (2017).

[65] Y. Schattner, S. Lederer, S. A. Kivelson, and E. Berg, Ising nematic quantum critical point in a metal: A monte carlo study, *Physical Review X* **6**, 10.1103/PhysRevX.6.031028 (2016).

[66] T. Sato, M. Hohenadler, and F. F. Assaad, Dirac fermions with competing orders: Non-landau transition with emergent symmetry, *Phys. Rev. Lett.* **119**, 197203 (2017).

[67] G. Pan, W. Wang, A. Davis, Y. Wang, and Z. Y. Meng, Yukawa-syk model and self-tuned quantum criticality, *Phys. Rev. Research* **3**, 013250 (2021).

[68] W. Wang, A. Davis, G. Pan, Y. Wang, and Z. Y. Meng, Phase diagram of the spin- $\frac{1}{2}$ yukawa-sachdev-ye-kitaev model: Non-fermi liquid, insulator, and superconductor, *Phys. Rev. B* **103**, 195108 (2021).

[69] G. Pan and Z. Y. Meng, Sign Problem in Quantum Monte Carlo Simulation, arXiv e-prints , arXiv:2204.08777 (2022), arXiv:2204.08777 [cond-mat.str-el].

[70] J. McMinis and N. M. Tubman, Renyi entropy of the interacting fermi liquid, *Physical Review B* **87**, 10.1103/PhysRevB.87.081108 (2013).

[71] J. Shao, E. A. Kim, F. D. Haldane, and E. H. Rezayi, Entanglement entropy of the $n=1/2$ composite fermion non-fermi liquid state, *Phys Rev Lett* **114**, 206402 (2015).

[72] R. V. Mishmash and O. I. Motrunich, Entanglement entropy of composite fermi liquid states on the lattice: In support of the widom formula, *Physical Review B* **94**, 10.1103/PhysRevB.94.081110 (2016).

[73] T. Grover, Y. Zhang, and A. Vishwanath, Entanglement entropy as a portal to the physics of quantum spin liquids, *New Journal of Physics* **15**, 025002 (2013).

[74] P. Broecker and S. Trebst, Rényi entropies of interacting fermions from determinantal quantum monte carlo simulations, *Journal of Statistical Mechanics: Theory and Experiment* **2014**, P08015 (2014).

[75] D. A. Abanin and E. Demler, Measuring entanglement entropy of a generic many-body system with a quantum switch, *Phys Rev Lett* **109**, 020504 (2012).

[76] A. J. Daley, H. Pichler, J. Schachenmayer, and P. Zoller, Measuring entanglement growth in quench dynamics of bosons in an optical lattice, *Phys Rev Lett* **109**, 020505 (2012).

[77] R. Islam, R. Ma, P. M. Preiss, M. E. Tai, A. Lukin, M. Rispoli, and M. Greiner, Measuring entanglement entropy in a quantum many-body system, *Nature* **528**, 77 (2015).

[78] Y. Liu, W. Jiang, A. Klein, Y. Wang, K. Sun, A. V. Chubukov, and Z. Y. Meng, Dynamical exponent of a quantum critical itinerant ferromagnet: A monte carlo study, *Phys. Rev. B* **105**, L041111 (2022).

[79] W. Jiang, Y. Liu, A. Klein, Y. Wang, K. Sun, A. V. Chubukov, and Z. Y. Meng, Monte carlo study of the pseudogap and superconductivity emerging from quantum magnetic fluctuations, *Nature Communications* **13**, 2655 (2022).

[80] X. Zhang, G. Pan, Y. Zhang, J. Kang, and Z. Y. Meng, Momentum space quantum monte carlo on twisted bilayer graphene, *Chinese Physics Letters* **38**, 077305 (2021).

[81] G. Pan, X. Zhang, H. Li, K. Sun, and Z. Y. Meng, Dynamical properties of collective excitations in twisted bilayer graphene, *Phys. Rev. B* **105**, L121110 (2022).

[82] X. Zhang, K. Sun, H. Li, G. Pan, and Z. Y. Meng, Superconductivity and bosonic fluid emerging from moiré flat bands, *Phys. Rev. B* **106**, 184517 (2022).

[83] B.-B. Chen, Y. D. Liao, Z. Chen, O. Vafek, J. Kang, W. Li, and Z. Y. Meng, Realization of topological mott insulator in a twisted bilayer graphene lattice model, *Nature Communications* **12**, 5480 (2021).

[84] X. Lin, B.-B. Chen, W. Li, Z. Y. Meng, and T. Shi, Exciton proliferation and fate of the topological mott insulator in a twisted bilayer graphene lattice model, *Phys. Rev. Lett.* **128**, 157201 (2022).

[85] X. Y. Xu, Y. Qi, L. Zhang, F. F. Assaad, C. Xu, and Z. Y. Meng, Monte carlo study of lattice compact quantum electrodynamics with fermionic matter: The parent state of quantum phases, *Phys. Rev. X* **9**, 021022 (2019).

[86] W. Wang, D.-C. Lu, X. Y. Xu, Y.-Z. You, and Z. Y. Meng, Dynamics of compact quantum electrodynamics at large fermion flavor, *Phys. Rev. B* **100**, 085123 (2019).

[87] L. Janssen, W. Wang, M. M. Scherer, Z. Y. Meng, and X. Y. Xu, Confinement transition in the $q\text{ed}_3$ -gross-neveu-xy universality class, *Phys. Rev. B* **101**, 235118 (2020).

[88] Y. Da Liao, X. Y. Xu, Z. Y. Meng, and Y. Qi, Dirac fermions with plaquette interactions. ii. su(4) phase diagram with gross-neveu criticality and quantum spin liquid, *Phys. Rev. B* **106**, 115149 (2022).

[89] Z. H. Liu, M. Vojta, F. F. Assaad, and L. Janssen, Metallic and deconfined quantum criticality in dirac systems, *Phys. Rev. Lett.* **128**, 087201 (2022).

[90] Z. Wang, M. P. Zaletel, R. S. K. Mong, and F. F. Assaad, Phases of the (2 + 1) dimensional so(5) nonlinear sigma model with topological term, *Phys. Rev. Lett.* **126**, 045701 (2021).

[91] Z. Wang, Y. Liu, T. Sato, M. Hohenadler, C. Wang, W. Guo, and F. F. Assaad, Doping-induced quantum spin hall insulator to superconductor transition, *Phys. Rev. Lett.* **126**, 205701 (2021).

[92] Y. Liu, Z. Wang, T. Sato, M. Hohenadler, C. Wang, W. Guo, and F. F. Assaad, Superconductivity from the condensation of topological defects in a quantum spin-hall insulator, *Nature Communications* **10**, 2658 (2019).

[93] Y. Da Liao, X. Y. Xu, Z. Y. Meng, and Y. Qi, Dirac fermions with plaquette interactions. i. su(2) phase diagram with gross-neveu and deconfined quantum criticalities, *Phys. Rev. B* **106**, 075111 (2022).

[94] Y. Da Liao, X. Y. Xu, Z. Y. Meng, and Y. Qi, Dirac fermions with plaquette interactions. iii. $SU(n)$ phase diagram with gross-neveu criticality and first-order phase transition, *Phys. Rev. B* **106**, 155159 (2022).

[95] T. Giamarchi, *Quantum Physics in One Dimension* (Clarendon Press, 2004).

[96] E. Fradkin, *Field Theories of Condensed Matter Physics*, 2nd ed. (Cambridge University Press, 2013) pp. 145–188.

[97] J. Voit, One-dimensional Fermi liquids, *Rep. Prog. Phys.* **58**, 977 (1995).

[98] A. W. Sandvik, L. Balents, and D. K. Campbell, Ground state phases of the half-filled one-dimensional extended hubbard model, *Phys. Rev. Lett.* **92**, 236401 (2004).

[99] S. Ejima and S. Nishimoto, Phase diagram of the one-dimensional half-filled extended hubbard model, *Phys. Rev. Lett.* **99**, 216403 (2007).